Dynamic contribution of recycled components from the subducted Pacific slab: Oxygen isotopic composition of the basalts from 106 Ma to 60 Ma in North China Craton

Jia Liu, Zi-Zhen Wang, Hao-Ran Yu, Qun-Ke Xia, Etienne Deloule, Min Feng

AGU PUBLICATIONS

JGR

Journal of Geophysical Research: Solid Earth

RESEARCH ARTICLE
10.1002/2016JB013156

Key Points:
- The $\delta^{18}O$ of the 106–60 Ma basalts in NCC were measured by SIMS
- The $\delta^{18}O$ of the basalts are different from that of the lithospheric mantle
- OIB-type rocks in NCC were most likely derived from the convective asthenosphere, rather than the lithospheric mantle

Supporting Information:
- Supporting Information S1
- Data Set S1
- Data Set S2

Correspondence to:
J. Liu,
liujia08@ustc.edu.cn

Citation:
Liu, J., Z.-Z. Wang, H.-R. Yu, Q.-K. Xia, E. Deloule, and M. Feng (2017), Dynamic contribution of recycled components from the subducted Pacific slab: Oxygen isotopic composition of the basalts from 106 Ma to 60 Ma in North China Craton, *J. Geophys. Res. Solid Earth*, *122*, 988–1006, doi:10.1002/2016JB013156.

Received 7 MAY 2016
Accepted 29 JAN 2017
Accepted article online 1 FEB 2017
Published online 18 FEB 2017

Dynamic contribution of recycled components from the subducted Pacific slab: Oxygen isotopic composition of the basalts from 106 Ma to 60 Ma in North China Craton

Jia Liu[1], Zi-Zhen Wang[1], Hao-Ran Yu[1], Qun-Ke Xia[2], Etienne Deloule[3], and Min Feng[1]

[1]CAS Key Laboratory of Crust-Mantle Materials and Environments, School of Earth and Space Science, University of Science and Technology of China, Hefei, China, [2]School of Earth Sciences, Zhejiang University, Hangzhou, China, [3]CRPG, UMR 7358, CNRS, Université de Lorraine, Vandoeuvre-les-Nancy, France

Abstract How the materials derived from the stagnant Pacific slab contributed to the mantle sources of the mafic rocks in east China is still in hot debate. In this work, $\delta^{18}O$ (Vienna standard mean ocean water) values of clinopyroxene phenocrysts in the oceanic island basalts (OIB)-type mafic rocks from 106 Ma to 60 Ma in the east North China Craton (NCC) were measured by secondary ion mass spectrometry. Our data show that for all of the samples, the $\delta^{18}O_{cpx}$ are dominantly higher than that of the clinopyroxene from normal mid-oceanic ridge basalt (5.4–5.8‰), which confirms the role of recycled oceanic crust (ROC) in their mantle sources. Combining the $\delta^{18}O$ data of basalts and the lithospheric mantle in the literature, we found that in the southeast NCC, upper and lower ROC components alternately appeared in the mantle sources of basalts, but these ROC components are consistently different from that in the lithospheric mantle, while in the northern NCC, the recycled components in the sources seem to be persistently from upper ROC. These observations suggest that (1) these mafic OIB-type rocks are most likely derived from the convective asthenosphere and (2) the contribution of components from the Pacific oceanic slab into the NCC upper mantle was dynamic, without a simple temporal trend. This new knowledge calls for the reconsideration of the existing models of the thinning process of the NCC lithospheric mantle, and it warns against simply using the chemical composition of basalts to infer the evolution of lithosphere.

1. Introduction

Many seismic tomography studies have shown that the subducted Pacific oceanic slab has been stagnant within the mantle transition zone and has extended westward subhorizontally beneath East Asia [*Fukao et al*., 1992; *Huang and Zhao*, 2006]. The western end of this stagnant slab has reached the North-South Gravity Lineament (NSGL) [*Huang and Zhao*, 2006]. The subduction of the Pacific plate and the subsequent extension is now regarded as one of the principal triggers of the destruction of the North China Craton (NCC) [*Xu*, 2007; *Zhu et al*., 2011]. In addition to the dynamic impact, such as inducing the rift of the lithospheric mantle and the subsequent upwelling of asthenosphere, many studies have suggested that the components (hydrated fluids and/or melts) derived from this subducted oceanic slab have directly contributed to the metasomatism and thinning of the lithospheric mantle and/or the production of the mafic magmatism from the Early Cretaceous to the late Cenozoic [*Niu*, 2005; *Zhao*, 2004; *Pang et al*., 2015; *Meng et al*., 2015; *Xia et al*., 2013; *Zhang et al*., 2009; *Wang et al*., 2011; *Z. Xu et al*., 2012; *Y. G. Xu et al*., 2012; *Yang et al*., 2012; *Sakuyama et al*., 2013; *Liu et al*., 2015a, 2015b; *Chen et al*., 2015; *Wang et al*., 2015; *Xu*, 2014; *Kuang et al*., 2012].

Recently, the role of the dehydrated fluids from the subducted Pacific slab in the thinning of the SCLM has been shown by quantitative or qualitative determinations of the water concentration of the lithospheric mantle during the Early Cretaceous [*Xia et al*., 2013; *Liu et al*., 2016; *Pang et al*., 2015]. However, whether and how the slab-derived components were associated with the mantle sources of the Late Cretaceous to Cenozoic basalts are still under debate. *Niu* [2005], *Guo et al*. [2014], and *Meng et al*. [2015] strengthened the role of hydrous melts released from the subducted Pacific slab as the metasomatic agents for the mantle sources of the mafic rocks with ages $<$110 Ma, while they denied the contribution of recycled subducted marine carbonates and partial melts of the basaltic oceanic crust. In contrast, *Zhang et al*. [2009], *Wang et al*. [2011], and *Z. Xu et al*. [2012] argue that the $\delta^{18}O$ anomaly (which is generally lower than the $\delta^{18}O$ for N-MORB olivine, 5.16 ± 0.09‰ [*Eiler et al*., 1997]) of the olivine and pyroxene phenocrysts in the late Cenozoic basalts in the

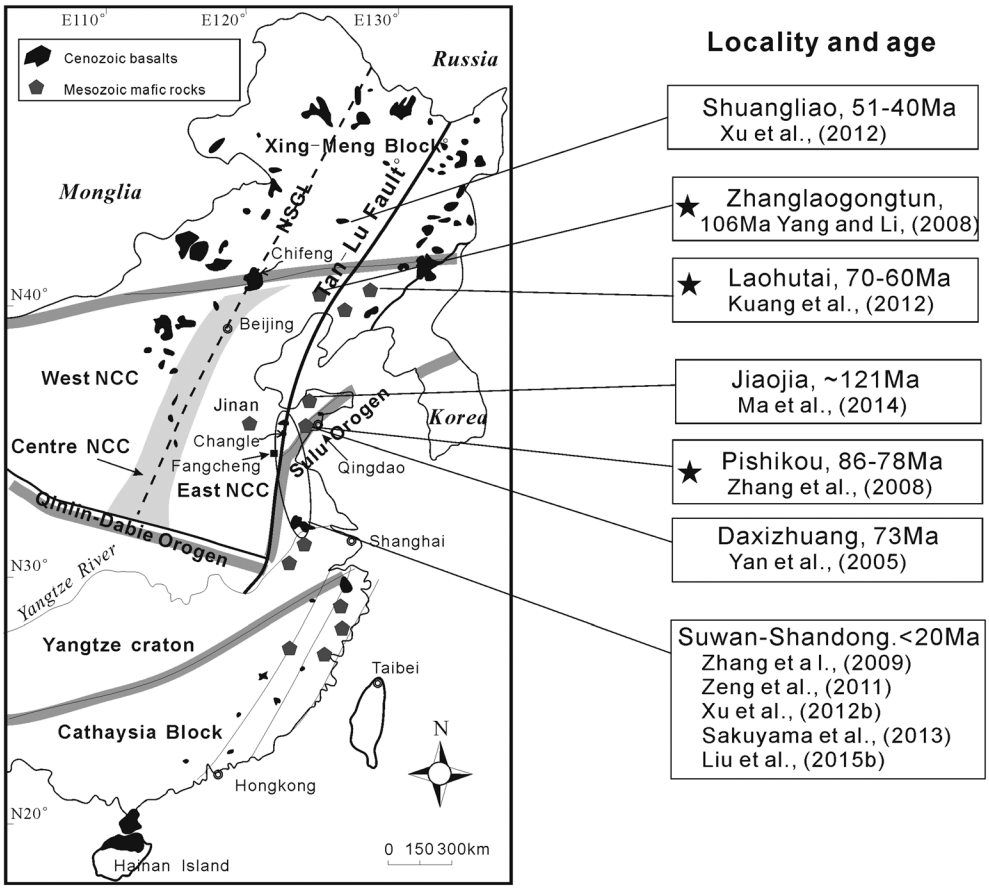

Figure 1. The simplified tectonic scheme for east China and the location of the 121 Ma to late Cenozoic basalts. NSGL represent the North-South Gravity Lineament. The dark stars mark the basalts in this study.

southeast NCC exclusively provides evidence for the involvement of components derived from the subducted oceanic crust. They further suggest that these recycled oceanic components had resided in a juvenile lithospheric mantle (formed by cooling of the upwelling asthenosphere) since the Early Cretaceous in the form of pyroxenites that were the product of the interaction between the peridotite and ROC-derived melts. However, very recently, *Y. G. Xu et al.* [2012], *Kuang et al.* [2012], and *Xu* [2014] investigated the temporal changes of geochemical compositions, such as Eu/Eu* and $^{87}Sr/^{86}Sr$, for the basalts from 90 to 40 Ma in the eastern NCC, and they attributed the secular shifts of the geochemical characteristics to the differential melting of the recycled components from the upper to lower ROC in the upwelling asthenosphere.

The principal sensitivity to the interaction of rocks with the Earth's hydrosphere makes oxygen isotope geochemistry a sensitive tool for identifying recycled crustal material from mantle-derived rocks and minerals [e.g., *Muehlenbachs*, 1986; *Eiler*, 2001]. In this work, using secondary ion mass spectrometry (SIMS), we measured the oxygen isotopes of clinopyroxene (cpx) phenocrysts in 106 Ma to 60 Ma basalts from the west Liaoning and east Shandong region (Figure 1). We also compiled the oxygen isotopic data for the lithospheric mantle of the eastern NCC from the Early Cretaceous to late Cenozoic and compared them to the $\delta^{18}O$ data of basalts from this work and from the literature. The results will help us to explore (1) whether there were recycled oceanic crust components in the mantle sources of mafic rocks during the Late Cretaceous to early Cenozoic, (2) whether there was a temporal or regional variation for these ROC components, and (3) whether these ROC components resided in the juvenile lithospheric mantle since the Early Cretaceous or were incorporated into the upper mantle gradually on a long time scale. The answers to these questions would (1) improve our understanding of the recycling process of a subducted oceanic slab in the "back-arc" region and (2) provide new insight in the discussion of the thinning process of the NCC lithospheric mantle.

2. Geological Background and Samples in This Study

2.1. Mafic Magmatism From Mesozoic to Cenozoic in NCC

The NCC has been stable since its cratonization [*Zhao and Zhai*, 2013] in the Proterozoic. Extensive basaltic magmatism occurred from the Mesozoic on and can be divided into three stages, after *Xu et al*. [2009]. The first stage of magmatism is from the Late Jurassic and Early Cretaceous and is distributed both in the margin and interior of the NCC. This basaltic magmatism is characterized by a very negative εNd(t) value (down to −20) and an arc-type trace element pattern in the primitive mantle normalized diagram, which has been suggested to be derived from the enriched lithospheric mantle [*Xu*, 2001; *Zhang et al*., 2002; *Yang and Li*, 2008; *Huang et al*., 2012]. However, a recent study on an Early Cretaceous (~121 Ma) lamprophyre in the Jiaodong Peninsula shows εNd(t) up to 1.76 and OIB-type trace element patterns [*Ma et al*., 2014]. The second stage of magmatism is from ~106 to 40 Ma [*Zhang et al*., 2003; *Yang and Li*, 2008; *Yan et al*., 2005; *Zhang et al*., 2008; *Kuang et al*., 2012; *Z. Xu et al*., 2012; *Cai et al*., 2013; *Xu*, 2014]. These basalts have positive εNd(t) values but more varied $^{87}Sr/^{86}Sr$ and OIB-type trace element patterns, and they show temporal variations in their Eu/Eu* and $^{87}Sr/^{86}Sr$ ratios [*Z. Xu et al*., 2012; *Xu*, 2014; *Kuang et al*., 2012]. The third stage of magmatism is in the late Cenozoic. The basalts in this stage include predominantly alkali basalts and subordinate basanites and tholeiites. The obvious features of these basalts are positive εNd(t) values and OIB-type trace element patterns [*Song et al*., 1990; *Zhi et al*., 1990; *Zhang et al*., 2009; *Zeng et al*., 2011]. Recently, it has been suggested that the component from ROC or recycled continental crust exists in their mantle source, despite the fact that there is still debate about whether the mantle source resides in the asthenosphere or in the lithospheric mantle [*Liu et al*., 2008; *Zhang et al*., 2009; *Zeng et al*., 2011; *Z. Xu et al*., 2012; *Y. G. Xu et al*., 2012; *Sakuyama et al*., 2013; *Liu et al*., 2015a, 2015b]. Such a secular variation in magma composition was recently suggested to reflect the prolonged thinning of the NCC lithospheric mantle [*Z. Xu et al*., 2012; *Xu*, 2001, 2014; *Kuang et al*., 2012].

2.2. Samples in This Study: 106 Ma to 60 Ma Basalts in NCC

In this work, a subset of second-stage mafic rocks from *Xu* [2014], nominally the Pishikou basanites, Laohutai alkali-to-tholeiitic basalts [*Kuang et al*., 2012], and Zhanglaogongtun alkali basalts (106 Ma, the first-appeared basalt with OIB-type trace element pattern and εNd(t) >0 in the northern margin of the NCC [*Zhang et al*., 2003; *Yang and Li*, 2008]) (Figure 1 and supporting information Data Set S1), was chosen for analysis of their oxygen isotopic composition. A brief description of these rocks is given below in the order of decreasing age of eruption, and their geochemical characteristics are shown in Figure 2.

The Zhanglaogongtun Formation (ZLGT) alkali basalts erupted at 106 Ma (Figure 1), and they are dark gray and massive with well-developed columnar jointing [*Zhang et al*., 2003; *Yang and Li*, 2008]. Most of the samples contain sparse olivine and plagioclase phenocrysts and possess small spinel-facies mantle xenoliths [*Zhang et al*., 2003] and crustal-derived cpx xenocrysts as the core of some of the zoned cpx (this work; see Figure 3). In this work, a subset of the samples from *Yang and Li* [2008] (JG1-4) are selected. These sample suites have also been measured for Mg isotopic composition by *Yang et al*. [2012].

The Pishikou (PSK) dikes, with K-Ar ages from 86 to 78 Ma, intruded into the Laoshan Early Cretaceous alkali granites near Qingdao in Jiaodong Peninsula [*Zhang et al*., 2008]. The dike is approximately 5–6 m wide and can be subdivided into the southern and northern parts. The samples in this study were sampled from the southern part, which contains abundant peridotite and granulite xenoliths. All samples are dark green and show porphyritic texture. Phenocrysts are small and dominantly clinopyroxene (cpx, ~10%), and the matrix is composed of clinopyroxene, feldspar, aphanitic materials, and some accessory minerals of ilmenites and apatites. Cpx phenocrysts are usually zoned, with the core as mantle- or crustal-derived xenocrysts and rim growing from the magma (see section 4). The $\delta^{18}O$ of olivine as xenocrysts or in peridotite xenoliths hosted by these basanites have been measured by *Guo et al*. [2013] with secondary ion mass spectrometer (SIMS).

The Laohutai (LHT) Formation is located in the Fushun-Mishan graben near Fushun City, which is the northern extension of the Tan-Lu fault. It consists of volcanic successions and subordinate amounts of coal, gray to black shales, sandstones, and tuffs. The volcanic lava succession could be subdivided into three units, in which the lowermost is alkali basalts and the middle and upper units are tholeiitic basalts [*Kuang et al*., 2012]. Ar-Ar dating shows that they were emplaced at 70 Ma (alkali basalts) and 60 Ma

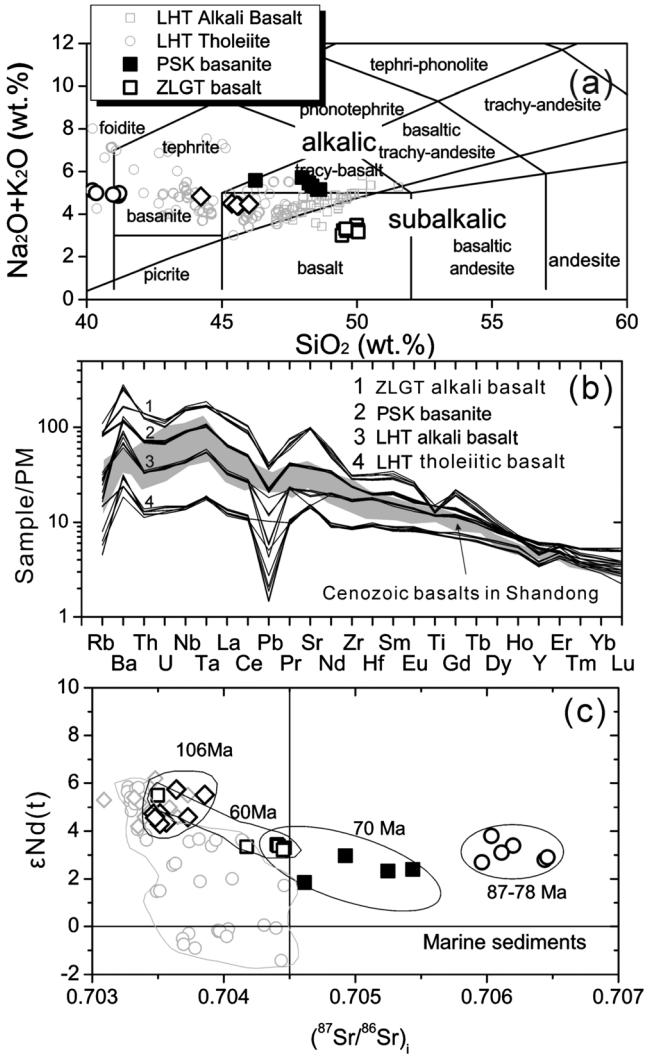

Figure 2. Major, trace and Sr-Nd isotopic characteristics of the 106–60 Ma basalts in this study. LHT represents Laihutai, PSK represents Pishikou, and ZLGT represents Zhanglaogongtun. The data source of these basalts can be found in the main text. (a) Total alkali versus SiO_2 plots. Mafic rocks erupted in Late Cretaceous (thin gray square, data from *Zhang et al*. [2002] and *Gao et al*. [2008]) and late Cenozoic basalts (thin gray circle) are also shown for comparison. (b) Primitive mantle normalized trace element patterns. The late Cenozoic basalts in Shandong [*Zeng et al*., 2011] are shown in the gray region. (c) Sr-Nd isotopes. Thin gray circles are late Cenozoic basalts in Shandong [*Zeng et al*., 2011]. The PM normalization value is from *Mcdonough and Sun* [1995].

(tholeiitic basalts) [*Kuang et al*., 2012]. The basalts are black and massive. The phenocrysts are olivine (<2%) and augite (5–10%), and the groundmass is composed of plagioclase (20–40%), pyroxene (30–40%), and minor olivine and magnetite. In this study, a subset of alkali basalts (LHT1, LHT9, and LHT19) and tholeiitic basalts (LHT20 and LHT25) from *Kuang et al*. [2012] was chosen. Note that *Kuang et al*. [2012] did not publish any geochemical data for sample LHT19, and its rock type was determined by comparison of the trace element patterns of cpx phenocrysts from this sample and other type-known samples (see supporting information Figure S1 for details).

3. Analysis Methods

Following the procedure of *Liu et al*., [2015a, 2015b], we used secondary ion mass spectrometry (SIMS) to measure the $\delta^{18}O$ value of the cpx phenocrysts in these basalts. Compared with the laser fluorination method (LF), this approach allows us to avoid the bias caused by alteration as much as possible. In addition, the reason for our preference for cpx phenocrysts rather than olivine is that (1) olivine phenocrysts in some of our samples are rather sparse and (2) the matrix effect during the SIMS analysis for cpx could be more accurately constrained than for olivine. The rock samples were first cut and polished into double-polished thin sections (~150 μm thick), and then Fourier transform infrared spectrometry analysis was performed to examine the alteration and small melt or fluid inclusions [*Liu et al*., 2015a]. Cpx separates without alteration-contaminants and free of inclusions were mounted again for chemical composition and oxygen isotope analysis.

3.1. Electron Microprobe

The chemical compositions of cpx phenocrysts were measured with a Shimadzu Electron Probe Microanalyzer (EPMA 1600) at CAS-CMME, USTC. Backscattered Electron (BSE) images were used to check the homogeneity of these phenocrysts. During the quantitative analysis, the operating conditions were set as follows: 15 kV accelerating voltage, 20 nA beam current, and <5 μm beam diameter. Natural minerals and synthetic oxides were used as standards, and the ZAF procedure was used for data correction. A portion of the Electron Microprobe (EMP) analyses was conducted with a JEOL at Hefei University of Technology.

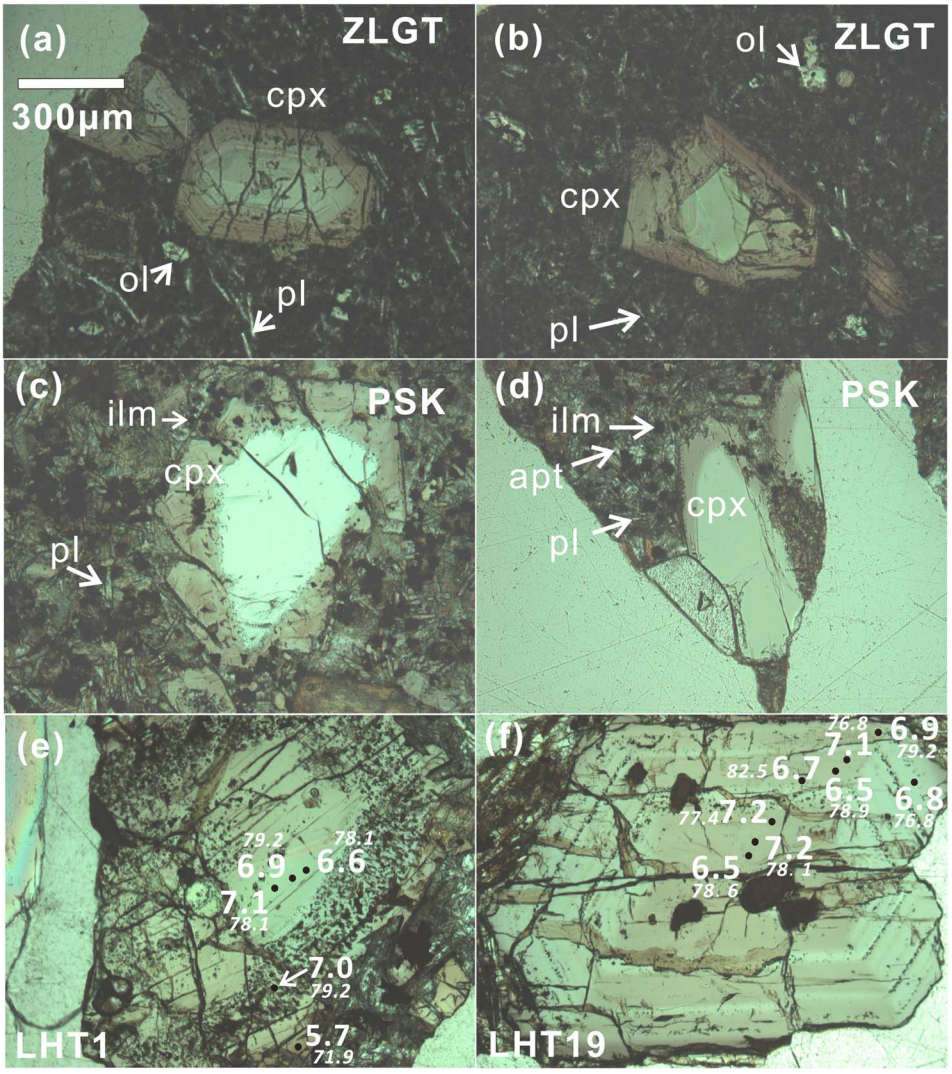

Figure 3. Petrologic photograph of clinopyroxene phenocrysts in the studied samples. All of the photographs are taken under plane-polarized light, and all slices have an approximate thickness of 100 μm. The dimensions for all photos are the same to that shown in Figure 3a. (a and b) Zoned cpx in Zhanglaogongtun (ZLGT) basalts. In Figure 3a, the core is magmatic and has higher Mg# than the rim, while in Figure 3b the core is crustal-derived xenocryst. (c and d) Zoned cpx in Pishikou (PSK) basanite. The cores are all crustal xenocrysts. The comparison of chemical composition of the cores and igneous rims is shown in Figure 4. (e and f) Cpx phenocrysts from Laohutai alkali basalts. The dark spots show the positions of SIMS analyses. The white bold numbers show the $\delta^{18}O$ values from secondary ion mass spectrometer (SIMS) analyses, and the italic small white numbers are the Mg# of the cpx analysis spots. Abbreviations: apt, apatite; ilm, ilmenite; pl, plagioclase.

Analytical conditions are similar to that at USTC. Cross comparison of the results from these two labs show that there are no systematic differences. The BSE images and Mg# calculated from the point-by-point data were used to identify the zonation and xenocrystic cores for all of the cpx families.

3.2. In Situ SIMS

The ion microprobe analyses were carried out using the CRPG-CNRS Cameca IMS-1280 instrument at Nancy (undated from IMS-1270). The analysis details are the same as in *Liu et al.* [2015a]. Four cpx megacrysts (NSH14, 2, 5, and 8) from the Nushan basanite, eastern China, with Mg# from 71.6 to 80.3 [*Xia et al.*, 2004], were used as standards to correct for the matrix effect. In each mount, a piece of cpx megacryst NSH6 (with an Mg# of 75.9) was measured in bracket to trace the possible instrumental drift. All of the

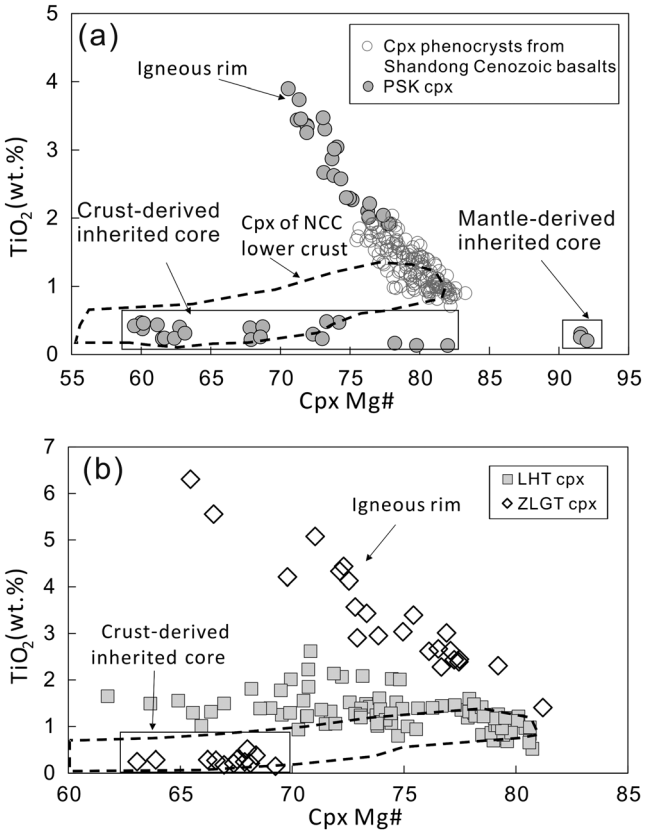

Figure 4. (a and b) TiO_2 versus Mg# plots for the cpx in the studied samples. The compositions of the cpx cores shown in Figure 3 are marked by real rectangles. In Figure 4a, the cpx phenocrysts from the late Cenozoic alkali basalts in Shandong are also plotted for comparison (data from *Liu et al.* [2015b]). The dashed lines mark the composition region of the cpx from the lower continental crust in NCC (data from *Zhang et al.* [2008, and references therein]).

mounts were coated with Au to prevent charging. An approximately 5–8 nA, 10 kV Cs^+ primary ion beam current was used in focused mode, with a spot size of approximately 20 μm. The incidence of an electron flood gun was used to compensate for any sample charging. The secondary O^- ions were accelerated at 10 kV and analyzed at a mass resolution power of 3000, to resolve the ^{17}OH isobaric interference on ^{18}O. Oxygen isotopes were measured in multicollection mode, using two off-axis Faraday cups, L'2 for ^{16}O, and H1 for ^{18}O. Each analysis takes approximately 4 min, including 60 s of presputtering, ~40 s of automated centering and 150 s of integrating oxygen isotope signals. The internal precision for one spot analysis was typically better than 0.1‰ (2σ). For each cpx grain, three to eight spots were analyzed. The "matrix" effect, as described by *Gurenko et al.* [2001], was taken into account when using the correlation of instrumental mass fractionations (IMF) relative to the Mg# (Mg# = Mg/(Mg + Fe) mol) of the reference cpx (see supporting information Figure S2 for the calibration lines). The reproducibility of $\delta^{18}O$ during a single analytical session (1 day) based on replicate analyses of standards is ~0.40‰ (2 SD). When the average of the analyses on one cpx grain are reported as the $\delta^{18}O$ of that grain, the standard error of the mean are better than 0.3‰ (2 SE).

4. Results

4.1. Major Element Composition of Clinopyroxene Phenocrysts

The major element data of cpx phenocrysts are listed in supporting information Data Set S2. For the ZLGT alkali basalt, the cpx phenocrysts are usually chemically zoned. According to the differences in chemical composition and crystal form, the cpx cores could be classified in two groups: (1) In group 1, the cores are irregular and anhedral, their Mg# are lower than 70 (62–69), and their TiO_2 contents are lower than 0.5 wt %, which is consistent with the chemical composition of the cpx from the NCC lower continental crust (Figure 4a); (2) and in group 2, the cores are euhedral, and their TiO_2-Mg# plot shows the same trend defined by their igneous overgrowth rims (Figure 4a), which indicates that they are the early crystallized magmatic phenocrysts. Overall, the cpx crystallized from the magma is augitic to diopsidic, with Mg# from 82.4 to 65.4. For the cpx phenocrysts in the PSK basanites, the situation is similar to that of the ZLGT alkali basalts. Nearly all of the cpx phenocrysts have core-rim zoning, while the cores are xenocrysts from granulites or lithospheric mantle. As shown in Figure 4b, the igneous cpx have distinctively higher TiO_2 contents, and their Mg# ranges from 77 to 69. For the LHT alkali basalts and tholeiites, all of the cpx has TiO_2 higher than 0.50 wt%, and this value increases with decreasing Mg# (Figure 4a) along a wide trend, which indicates that all of these cpx are igneous phenocrysts. For all samples from these three locations, the highest Mg# of

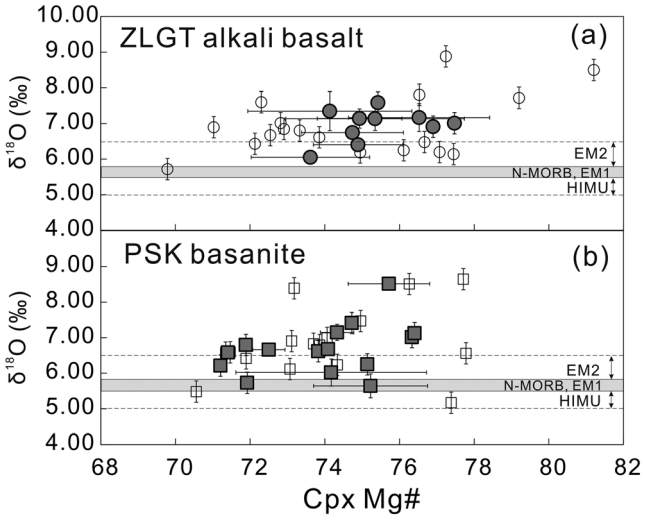

Figure 5. Oxygen isotope compositions of the cpx phenocrysts in the ZLGT and PSK basalts versus Mg#. The empty symbols are the $\delta^{18}O$ values for each single analysis spot, while the ones filled with dark gray color are the average for one specific cpx grain. The range of $\delta^{18}O$ values of cpx phenocrysts from N-MORB, EM1, EM2, and HIMU OIB, calculated from published $\delta^{18}O$ values of olivine phenocrysts [*Eiler et al*., 1997; *Widom and Farquhar*, 2003] and an equilibrium fractionation between cpx and olivine of 0.4%, is indicated by the gray bars or double headed arrows. The error bar for a single point $\delta^{18}O$ is taken as 0.3‰ (1 SD), while the error bar for the average $\delta^{18}O$ for one cpx grain varies from 0.14 to 0.4‰ (1 SE).

cpx is in equilibrium with the bulk rock if the Fe-Mg exchange coefficient (Kd) is assumed to be 0.275 ± 0.13 [*Putirka et al*., 2003].

4.2. Oxygen Isotopic Composition of Cpx Phenocrysts

The instrumental mass fractionation (IMF)-corrected oxygen isotope analyses of cpx phenocrysts (note that data for cpx xenocrysts and cpx with Mg# less than 70 are not shown) are plotted with Mg# in Figures 5 and 6, in which both the $\delta^{18}O$ of single points and the average for those in single grains are shown (Table 1). Overall, the main obvious characteristics of these $\delta^{18}O$ results are (1) oxygen isotopic compositions are rather heterogeneous, both on the intergrain and intragrain scale, and (2) except for very few spots (8 of 201 analyses) with $\delta^{18}O$ lower than 5.4‰, all other analyzed spots exhibit $\delta^{18}O$ higher than the normal mantle value (5.40–5.70‰ [*Mattey et al*., 1994; *Eiler et al*., 1997]). For the ZLGT alkali basalts, the cpx $\delta^{18}O$ values (5.74–8.88‰) are all higher than the values for cpx from N-MORB (5.70‰) and are similarly scattered in the Mg# range of 70 to 80 (Figure 5a). For the PSK samples, the single point $\delta^{18}O$ values vary from 5.48‰ to 8.64‰, except for one point with $\delta^{18}O$ of 5.17‰ (Figure 5b). For the LHT alkali basalts (LHT1, LHT9, and LHT19), the majority of the cpx suite $\delta^{18}O$ values are in the range of 5.67‰ to 8.02‰, while three cpx grains in LHT19 and LHT1 exhibit $\delta^{18}O$ slightly lower than the N-MORB value (Figures 6a and 6b). For the LHT tholeiitic basalts, all of the cpx grains exhibit $\delta^{18}O$ close to or higher than the N-MORB value (Figure 6c).

5. Discussion

5.1. Origin of the Oxygen Isotopic Anomaly

The $\delta^{18}O$ values of the cpx phenocrysts in all of these basalts (Figures 5 and 6) are dominantly higher than that of the cpx from typical MORBs and peridotite xenoliths (5.4–5.8‰ [*Mattey et al*., 1994; *Eiler et al*., 1997]), and many of them are even higher than cpx $\delta^{18}O$ from EM2-type OIB lavas (5.8–6.5‰ [*Eiler et al*., 1997; *Widom and Farquhar*, 2003]). The range of $\delta^{18}O$ for the cpx in one basalt sample is similar to that of the cpx phenocrysts in the Klyuchevskoy volcano, Kamchatka (5.5–8.0‰) (calculated from $\delta^{18}O$ of olivine phenocrysts and $\Delta^{18}O_{cpx\text{-}ol} = 0.4‰$ [*Auer et al*., 2009]). Due to the small fractionation between cpx phenocrysts and basaltic melt (~0.1‰, calculated from the $\Delta^{18}O_{cpx\text{-}ol} = 0.4‰$ and $\Delta^{18}O_{melt\text{-}ol} = \sim 0.4$ to 0.5‰ [*Eiler*, 2001]), the measured cpx $\delta^{18}O$ could be approximately considered as that of the basaltic melt. Multiple factors, such as magmatic processes (partial melting, fractional crystallization, and devolatilization), secondary alteration, and crustal contamination (or AFC processes), could change the primary oxygen isotopic composition of magma. In the following, the roles of these factors are discussed one by one.

A large number of natural observations and theoretical considerations show that for basaltic melts with MgO contents between 8 and 3 wt %, the partial melting, fractional crystallization, and devolatilization would not change the $\delta^{18}O$ of the magma to a level higher than 0.1‰ [*Eiler*, 2001, and references therein; *Zhao and Zheng*, 2003]. Thus, for our samples, their high bulk MgO contents (higher than 8 wt % [*Kuang et al*., 2012; *Yang and Li*, 2008; *Zhang et al*., 2008; this work]; see supporting information Data Set S1) would indicate

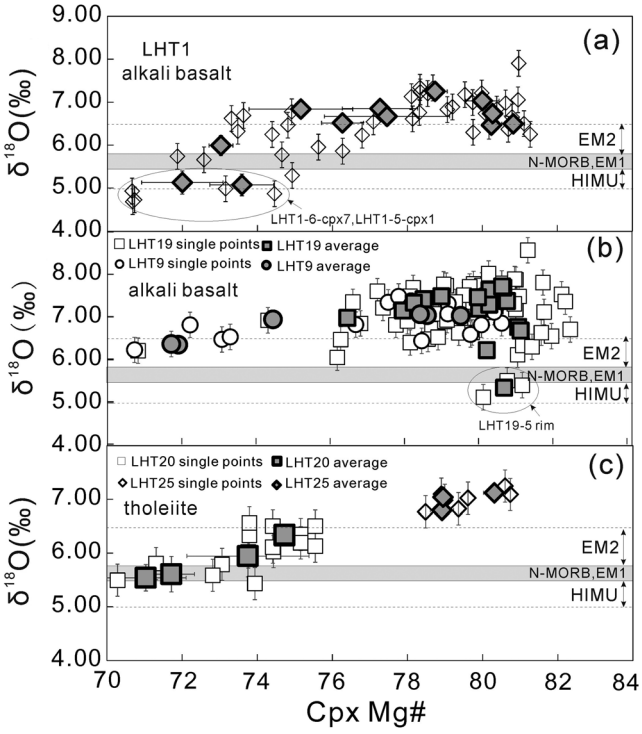

Figure 6. Oxygen isotope compositions of the cpx phenocrysts in the LHT alkali and tholeiitic basalts. The meaning of symbols and range of cpx from MORB and OIB are the same as in Figure 5. Note that most of the error bars (1 SE) of the grain average values are smaller than the scale of the symbols. The ellipses-marked analysis spots are that effected by mineral inclusions or the unperfect surface (see Figure S3).

that the oxygen anomaly were not caused by the simple magma evolution. In addition, the crustal contamination or assimilation also did not play a significant role. The bulk rock Ce/Pb and Nb/U ratios for the ZLGT, PSK, and LHT alkali basalts are ~25 and ~42, 19–24 and 40–46, and 27–70 and 32–40, respectively, which are consistent with the values for the global primary OIB and MORB basalts (Ce/Pb = 25 ± 5, Nb/U = 40 ± 7 [*Hofmann et al.*, 1986]). The bulk rock SiO_2 contents for the PSK basanites are 40–42 wt % (this study), and the bulk rock $^{87}Sr/^{86}Sr$ for LHT25 (tholeiite) is 0.70356 [*Kuang et al.*, 2012]. Overall, these indexes argue against a significant role of the continental crust, which has rather low Ce/Pb and Nb/U ratios, high SiO_2 content, and enriched radiogenic isotopes [*Rudnick and Gao*, 2003]. For the cpx within LHT20, combined with the sample LHT25 they constitute a trend in which the $\delta^{18}O$ decrease with decreasing of cpx Mg# (Figure 6c). However, these two samples have rather similar MORB and OIB-like Nb/U ratios (36.2 for LHT25 and 35.8 for LHT20, respectively), which indicate that the relatively low $\delta^{18}O$ (close to N-MORB value) could not be explained by the crustal assimilation of LHT25 magma. Instead, this apparent trend between Mg# and $\delta^{18}O$ would be explained by the fact that the cpx in LHT20 are crystallized from a melt with relatively low $\delta^{18}O$ and more evolution (like fractional crystallization of mafic minerals in the plumbing system). At last, for all of the samples, the high $\delta^{18}O$ values are not correlated with the LOI (loss on ignition) values of the bulk rocks, the grain sizes, or the cracks in the cpx grains (Figure 3), which indicate that water-rock interaction after magma eruption does not shift the $\delta^{18}O$ value of cpx. However, the few spot of SIMS analyses with $\delta^{18}O$ lower than 5.40‰ in sample LHT19 and LHT1 (Figures 6a and 6b) could be due to the contaminant of tiny mineral inclusions (see supporting information Figures S3d and S3f) and the relief or kink in the mineral rim caused by unperfected polishing (see supporting information Figure S3a).

Overall, we consider that the dominantly high $\delta^{18}O$, especially for the cpx with higher Mg#, reflects the signature of the primary magmas, and thus the characteristics of the mantle sources. The spread of $\delta^{18}O$ among cpx grains in a single basalt sample is similar to the case in the Taihang and Shandong Cenozoic basalts ($\delta^{18}O$ interval up to 2‰ in one basalt sample [*Liu et al.*, 2015a, 2015b]), the Canary Island basalts (La Gomera) [*Gurenko et al.*, 2011], the Borgarhraun basalt flow in northern Iceland [*Winpenny and Maclennan*, 2014], and the Chifeng Cenozoic continental flood basalts [*Wang et al.*, 2015], for which the $\delta^{18}O$ interval for minerals in one basalt sample could be up to 2‰. These types of heterogeneous $\delta^{18}O$ values were usually explained by a complex magma plumbing system for a very heterogeneous mantle-melting region [*Gurenko et al.*, 2011; *Winpenny and Maclennan*, 2014], which is not the main scope of this paper.

5.2. Recycled Oceanic Components in the Mantle Sources

According to the discussion above, the higher-than-normal mantle $\delta^{18}O$ values of the cpx phenocrysts in all of these basalts (Figure 5) were inherited from their parental magmas and, consequently, the mantle sources,

Table 1. The In Situ $\delta^{18}O$ of Cpx Phenocryst in the ZLGT, PSK, and LHT Basalts

Sample	Cpx Grain	Spot	Measured δ18O	1 SD	Mg#	IMF[a]	Drift[b]	δ18O Corrected	Average	1 SE
QDPS7	7-5-cpx2	1-1-3	5.54	0.10	75.1	−1.09	0.38	6.25	6.25	-
	7-4-cpx1	1-2-3	6.40	0.09	73.1	−0.78	0.28	6.91		
		1-2-4	6.12	0.11	71.9	−0.60	0.30	6.42	6.66	#NAME?
	7-3-cpx1	1-3-3	6.58	0.10	75.0	−1.06	0.17	7.47		
		1-3-4	6.15	0.10	73.7	−0.87	0.20	6.83	7.15	#NAME?
	7-4-cpx2	1-8-3	5.73	0.09	73.8	−0.89	0.00	6.62	6.62	-
QDPS5	5-1-cpx1	1-4-3	6.26	0.10	74.7	−1.03	−0.13	7.41	7.41	-
	5-2-cpx3	1-5-2	6.85	0.09	77.7	−1.48	−1.48	8.65		
		1-5-4	6.98	0.10	76.3	−1.26	−1.26	8.51		
		1-5-6	7.39	0.10	73.2	−0.79	−0.79	8.39	8.52	#NAME?
	5-1-cpx2	1-10-2	5.13	0.10	71.9	−0.60	0.00	5.73	5.73	-
	5-5-cpx1	1-11-2	5.27	0.13	74.3	−0.97	0.00	6.24		
		1-11-3	6.06	0.10	74.1	−0.93	0.00	6.99		
		1-11-4	5.89	0.12	73.9	−0.90	0.00	6.79	6.67	#NAME?
QDPS10	10-6-cpx1	1-17-3	5.84	0.10	76.4	−1.28	0.00	7.13	7.13	-
	10-6-cpx2A	1-18-1-2	5.74	0.12	71.9	−0.60	−0.43	6.80	6.80	-
	10-6-cpx2B	1-18-2-2	3.22	0.13	77.4	−1.43	−0.52	5.17		
		1-18-2-3	4.79	0.10	73.1	−0.78	−0.55	6.12	5.64	0.34
QDPS2	2-4-cpx2	1-6-3	5.72	0.10	71.2	−0.50	0.00	6.21	6.21	-
	2-6-cpx1	1-16-3	5.40	0.11	76.3	−1.27	−0.34	7.01	7.01	-
QDPS3	3-5-cpx1	1-15-1	4.71	0.10	70.6	−0.40	−0.37	5.48		
		1-15-2	4.67	0.08	77.8	−1.49	−0.40	6.56	6.02	0.38
QDPS9	9-6-cpx2	1-13-2	6.06	0.11	71.3	−0.52	0.00	6.58		
		1-13-3	6.05	0.08	71.5	−0.54	0.00	6.59	6.58	0.00
JG2	JG2-1-CPX1	5-1-1	6.06	0.10	76.5	−1.20	−0.54	7.80		
		5-1-4	5.56	0.10	73.3	−0.75	−0.50	6.80	7.14	0.27
	JG2-6-1	5-2-4	6.11	0.10	72.8	−0.67	−0.23	7.01		
		5-2-5	5.05	0.11	76.7	−1.22	−0.21	6.48	6.75	0.19
	JG2-3-1B	5-12-4	5.98	0.11	73.9	−0.82	0.19	6.61		
		5-12-5	6.32	0.09	79.2	−1.58	0.19	7.72	7.17	0.39
JG3	JG3-1-1	5-3-1-1	5.47	0.08	76.9	−1.25	−0.19	6.91	6.91	0.30
	JG3-7-1	5-4-1	6.64	0.11	81.2	−1.87	0.01	8.50		
		5-4-2	6.07	0.10	72.5	−0.63	0.03	6.67		
		5-4-3	7.06	0.09	72.3	−0.60	0.06	7.60	7.14	0.33
	JG3-4-2	5-5-2	6.26	0.13	72.9	−0.69	0.10	6.85		
		5-5-3	5.04	0.13	77.1	−1.28	0.12	6.20		
		5-5-4	4.95	0.09	77.5	−1.33	0.14	6.14		
		5-5-5	6.02	0.09	72.1	−0.57	0.17	6.43	6.40	0.14
	JG3-2-1	5-7-1	5.40	0.11	74.9	−0.98	0.21	6.19		
		5-7-3	5.34	0.09	76.1	−1.14	0.23	6.25	6.05	0.14
	JG3-1-2	5-8-2	6.88	0.10	75.4	−1.04	0.34	7.59	7.59	-
	JG3-1-3	5-11-1	5.86	0.11	77.5	−1.34	0.19	7.01	7.01	-
JG1	JG1-1-2	5-6-1	6.97	0.10	77.2	−1.30	−0.59	8.88		
		5-6-5	5.91	0.11	71.0	−0.42	−0.57	6.90	7.35	0.55
LHT1	LHT1-3-cpx5	2-11-1	4.75	0.09	80.79	−0.96	−0.95	6.66		
		2-11-2	4.60	0.07	80.18	−0.89	−0.95	6.44		
		2-11-3	4.50	0.08	79.75	−0.85	−0.95	6.30	6.47	0.09
	LHT1-2-cpx1	2-13-1	4.26	0.08	81.27	−1.01	−0.99	6.25		
		2-13-2	4.87	0.08	80.08	−0.88	−0.99	6.74		
		2-13-3	4.52	0.08	81.11	−0.99	−0.99	6.50	6.50	0.11
	LHT1-2-cpx1′	2-13-4	5.50	0.06	78.54	−0.72	−0.99	7.20		
		2-13-5	5.50	0.06	73.63	−0.20	−0.99	6.69		
		2-13-6	5.47	0.08	73.31	−0.17	−0.99	6.62	6.84	0.15
	LHT1-2-cpx3	2-12-1	4.99	0.09	77.09	−0.57	−0.99	6.54		
		2-12-2	4.71	0.09	76.79	−0.54	−0.99	6.23		
		2-12-3	5.45	0.08	74.91	−0.34	−0.99	6.78	6.52	0.13
	LHT1-3-cpx4	2-10-1	5.09	0.09	80.95	−0.97	−1.00	7.06		
		2-10-2	5.06	0.08	79.06	−0.77	−1.00	6.83		
		2-10-3	5.35	0.09	79.98	−0.87	−1.00	7.22	7.03	0.09
	LHT1-3-cpx4′	2-10-4	5.65	0.08	78.34	−0.70	−1.00	7.34		
		2-10-5	5.55	0.07	78.34	−0.70	−1.00	7.24		

Table 1. (continued)

Sample	Cpx Grain	Spot	Measured δ18O	1 SD	Mg#	IMF[a]	Drift[b]	δ18O Corrected	Average	1 SE
		2-10-6	5.36	0.09	79.53	−0.82	−1.00	7.18	7.25	0.04
	LHT1-6-cpx2	3-3-1	3.99	0.09	80.38	−1.71	−1.14	6.84		
		3-3-2	4.24	0.10	79.74	−1.61	−1.14	6.99		
		3-3-3	3.46	0.11	80.69	−1.76	−1.15	6.37	6.74	0.15
	LHT1-6-cpx2′	3-3-4	4.34	0.10	74.39	−0.74	−1.17	6.25		
		3-3-5	4.92	0.09	80.97	−1.80	−1.18	7.90	7.08	0.58
	LHT1-6-cpxX	3-2-2-1	4.02	0.10	72.57	−0.44	−1.19	5.66		
		3-2-2-2	4.54	0.09	73.48	−0.59	−1.20	6.33	5.99	0.24
	LHT1-6-cpxx	3-2-3-1	4.18	0.09	78.32	−1.38	−1.20	6.76		
		3-2-3-2	4.69	0.10	78.68	−1.43	−1.21	7.33		
		3-2-3-3	4.45	0.11	74.81	−0.81	−1.22	6.47	6.85	0.21
	LHT1-6-cpx7	3-1-1	3.73	0.09	74.65	−0.78	−1.26	5.78		
		3-1-2	3.58	0.09	70.66	−0.13	−1.22	4.93[c]		
		3-1-3	3.38	0.11	70.67	−0.14	−1.17	4.68[c]	5.13	0.27
	LHT1-5-cpx1	3-5-1	4.67	0.12	78.11	−1.34	−1.12	7.13		
		3-5-2	4.30	0.10	79.20	−1.52	−1.07	6.89		
		3-5-3	4.24	0.10	78.14	−1.35	−1.02	6.61		
		3-5-4	4.44	0.09	71.86	−0.33	−0.97	5.74		
		3-5-5	4.31	0.11	80.62	−1.75	−0.92	6.98	6.67	0.22
	LHT1-5-cpx4	3-4-1	4.24	0.12	75.62	−0.94	−0.77	5.95		
		3-4-2	4.03	0.10	76.27	−1.04	−0.78	5.86		
		3-4-3	3.68	0.13	74.93	−0.82	−0.79	5.29[c]	5.91	#NAME?
		3-4-4	3.32	0.10	74.45	−0.75	−0.80	4.86[c]		
		3-4-5	3.64	0.12	73.15	−0.54	−0.81	4.98[c]		
		3-4-6	3.76	0.12	70.72	−0.14	−0.82	4.72[c]		
LHT11	LHT11-cpxN1	3-6-1	4.02	0.12	79.43	−1.56	−1.11	6.69		
		3-6-2	4.40	0.09	79.49	−1.57	−1.11	7.08		
		3-6-3	4.67	0.10	79.49	−1.57	−1.12	7.36		
		3-6-4	4.15	0.09	79.07	−1.50	−1.13	6.77	6.97	0.13
LHT19	LHT19-5-cpx6	2-9-1	5.02	0.07	78.74	−0.74	−0.95	6.71		
		2-9-2	5.62	0.08	80.83	−0.96	−0.95	7.53		
		2-9-3	5.44	0.08	80.47	−0.92	−0.95	7.31	7.18	0.20
	LHT19-5-cpx6′	2-9-4	5.44	0.07	80.02	−0.87	−0.95	7.27		
		2-9-52-9-52-9-5	5.96	0.08	79.86	−0.86	−0.95	7.77		
		2-9-62-9-62-9-6	5.94	0.10	81.00	−0.98	−0.95	7.87	7.64	0.15
	LHT19-5 core	2-9-1-2	4.17	0.07	81.05	−0.98	−0.95	6.10		
		2-9-1-3	4.37	0.06	81.19	−1.00	−0.95	6.32	6.21	0.08
	LHT19-5 rim	2-9-1-4	3.27	0.07	80.13	−0.89	−0.95	5.11[c]		
		2-9-1-5	3.45	0.09	81.17	−1.00	−0.95	5.39[c]		
		2-9-1-6	3.60	0.08	80.77	−0.95	−0.95	5.50[c]	5.33	0.10
	LHT19-5-cpx1	2-7-2-1	5.14	0.12	80.61	−1.78	−0.48	7.40		
		2-7-2-2	5.00	0.11	80.47	−1.76	−0.48	7.24		
		2-7-2-3	5.07	0.09	79.78	−1.66	−0.48	7.21	7.28	0.05
	LHT19-5-cpx1′	2-7-2-4	5.17	0.10	79.76	−1.66	−0.48	7.31		
		2-7-2-5	5.66	0.09	76.61	−1.21	−0.48	7.35		
		2-7-2-6	5.53	0.08	80.62	−1.79	−0.48	7.79	7.48	0.12
	LHT19-5	2-7-1-1	4.09	0.08	81.96	−1.98	−0.48	6.54		
		2-7-1-2	4.52	0.10	79.47	−1.62	−0.48	6.62		
		2-7-1-3	4.69	0.10	81.76	−1.95	−0.48	7.11	6.76	0.15
	LHT19-5-cpx2	2-8-1	5.61	0.08	79.13	−1.57	−0.56	7.73		
		2-8-2	5.68	0.09	78.24	−1.44	−0.56	7.68		
		2-8-3	5.09	0.09	80.02	−1.70	−0.56	7.35		
		2-8-4	4.96	0.07	82.23	−2.02	−0.56	7.53		
		2-8-5	4.77	0.10	82.33	−2.03	−0.56	7.36		
		2-8-6	5.35	0.09	78.92	−1.54	−0.56	7.44		
		2-8-7	5.10	0.11	79.16	−1.58	−0.56	7.23		
		2-8-8	5.11	0.11	79.85	−1.68	−0.56	7.34	7.46	0.06
	LHT19-5-cpxN1	2-3-1	5.17	0.09	80.79	−1.81	−0.62	7.60		
		2-3-2	4.98	0.10	80.50	−1.77	−0.59	7.34		
		2-3-3	4.76	0.09	81.00	−1.84	−0.57	7.17	7.37	0.10
	LHT19-5-cpx4	2-4-1-1	5.48	0.10	80.09	−1.71	−0.55	7.74		

Table 1. (continued)

Sample	Cpx Grain	Spot	Measured δ18O	1 SD	Mg#	IMF[a]	Drift[b]	δ18O Corrected	Average	1 SE
		2-4-1-2	5.52	0.10	79.76	−1.66	−0.53	7.71		
		2-4-1-3	5.36	0.11	81.73	−1.94	−0.50	7.80		
		2-4-1-4	5.12	0.09	81.09	−1.85	−0.50	7.48	7.68	0.06
	LHT19-5-cpx5	2-6-1-1	5.66	0.10	78.14	−1.43	−0.40	7.48		
		2-6-1-2	5.05	0.10	77.77	−1.38	−0.38	6.81	7.14	0.24
	LHT19-5-cpx7	2-1-1	4.03	0.11	81.44	−1.90	−0.35	6.29		
		2-1-2	4.35	0.10	81.69	−1.94	−0.33	6.62		
		2-1-3	5.06	0.10	80.27	−1.73	−0.31	7.10	6.67	0.19
	LHT19-5-cpx4	2-2-1	5.18	0.11	80.96	−1.83	−0.29	7.30		
		2-2-2	6.02	0.11	80.27	−1.73	−0.26	8.02		
		2-2-3	5.78	0.11	74.32	−0.89	−0.24	6.91	7.41	0.26
	LHT19-5-cpx9	2-5-1-1	5.10	0.12	79.09	−1.57	−0.22	6.89		
		2-5-1-2	5.67	0.09	79.60	−1.64	−0.20	7.51		
		2-5-1-3	6.51	0.10	81.33	−1.89	−0.18	8.57		
		2-5-1-4	5.90	0.10	80.97	−1.83	−0.15	7.89	7.71	0.30
	LHT19-5-CPX8	4-14-1-1	6.36	0.08	77.27	−1.21	−0.03	7.60		
		4-14-1-2	5.68	0.12	78.13	−1.34	−0.02	7.04		
		4-14-1-3	5.80	0.09	79.37	−1.55	0.00	7.35	7.33	0.13
	LHT19-5-CPX8	4-14-2-1	6.28	0.10	79.06	−1.50	0.02	7.76		
		4-14-2-2	6.07	0.09	70.82	−0.16	0.03	6.20		
		4-14-2-3	5.44	0.08	79.52	−1.57	0.05	6.96	6.97	0.37
	LHT19	5-10-1	5.53	0.10	79.82	−1.67	0.57	6.63		
		5-10-2	5.49	0.11	78.15	−1.43	0.54	6.39		
		5-10-3	5.97	0.10	78.08	−1.42	0.50	6.90		
		5-10-4	5.75	0.10	76.28	−1.17	0.46	6.46		
		5-10-5	5.30	0.09	76.19	−1.15	0.42	6.04	6.48	0.13
	LHT19	5-9-1	5.40	0.11	78.64	−1.50	0.43	6.47		
		5-9-2	6.24	0.10	78.16	−1.43	0.45	7.23		
		5-9-3	6.35	0.10	77.42	−1.33	0.47	7.21		
		5-9-4	5.14	0.08	82.47	−2.05	0.49	6.70		
		5-9-5	5.49	0.10	78.91	−1.54	0.51	6.52		
		5-9-6	6.08	0.11	78.79	−1.52	0.54	7.07		
		5-9-7	5.90	0.11	79.15	−1.58	0.56	6.92		
		5-9-8	6.18	0.10	76.82	−1.24	0.58	6.84	6.87	0.10
LHT9	LHT9-CPX10	4-4-1	5.38	0.08	73.08	−0.53	−0.56	6.46		
		4-4-2	5.53	0.09	70.73	−0.14	−0.54	6.22	6.34	0.09
	LHT9-CPX11	4-3-1	5.27	0.08	79.18	−1.51	−0.52	7.31		
		4-3-2	5.51	0.11	78.18	−1.35	−0.51	7.37		
		4-3-3	4.54	0.09	78.47	−1.40	−0.49	6.43	7.04	0.25
	LHT9-CPX8	4-1-1-1	5.66	0.09	77.56	−1.25	−0.43	7.34		
		4-1-1-2	4.55	0.09	79.78	−1.61	−0.41	6.58		
		4-1-1-3	5.55	0.09	77.92	−1.31	−0.40	7.26	7.06	0.20
	LHT9-CPX8′	4-1-2-1	5.69	0.10	71.72	−0.30	−0.37	6.36	6.36	-
	LHT9-cpx7	3-11-1	5.02	0.12	73.31	−0.56	−0.94	6.52		
		3-11-2	5.23	0.10	77.84	−1.30	−0.95	7.48		
		3-11-3	5.46	0.10	72.22	−0.39	−0.96	6.81	6.94	0.23
	LHT9-cpx1	3-10-1	4.09	0.10	80.62	−1.75	−1.00	6.85		
		3-10-2	4.38	0.11	80.42	−1.72	−1.01	7.11		
		3-10-3	4.81	0.11	80.11	−1.67	−1.02	7.50		
		3-10-4	4.52	0.07	79.17	−1.51	−1.03	7.07		
		3-10-5	4.10	0.12	80.08	−1.66	−1.04	6.81		
		3-10-6	4.65	0.10	76.69	−1.11	−1.05	6.81	7.02	0.10
LHT20	LHT20-2-cpx3	4-6-1	4.63	0.09	74.43	−0.75	−0.65	6.03		
		4-6-2	4.63	0.10	73.06	−0.52	−0.64	5.79		
		4-6-3	4.76	0.09	73.76	−0.64	−0.62	6.02	5.95	0.06
	LHT20-1-cpx1	4-5-3	5.17	0.11	70.28	−0.07	−0.26	5.49		
		4-5-4	4.81	0.08	72.82	−0.48	−0.29	5.59	5.54	0.13
	LHT20-3-CPX3	4-7-1	4.96	0.10	71.31	−0.24	−0.61	5.81		
		4-7-2	4.99	0.08	69.90	−0.01	−0.59	5.59		
		4-7-3	4.19	0.07	73.94	−0.66	−0.57	5.43	5.61	0.09
	LHT20-4-CPXN1	4-11-1	5.41	0.09	74.41	−0.74	−0.35	6.50		

Table 1. (continued)

Sample	Cpx Grain	Spot	Measured δ18O	1 SD	Mg#	IMF[a]	Drift[b]	δ18O Corrected	Average	1 SE
		4-11-2	5.15	0.08	75.15	−0.86	−0.33	6.35		
		4-11-3	5.38	0.10	73.79	−0.64	−0.32	6.33		
		4-11-4	4.90	0.08	75.54	−0.93	−0.30	6.13	6.33	0.07
	LHT20-4-N2	4-8-1	5.19	0.08	74.41	−0.74	−0.18	6.11		
		4-8-2	5.17	0.07	75.15	−0.86	−0.16	6.19		
		4-8-3	5.77	0.10	73.79	−0.64	−0.15	6.56		
		4-8-4	5.45	0.09	75.54	−0.93	−0.13	6.50	6.34	0.10
LHT25	LHT25-1-cpx1	3-9-1	4.41	0.09	79.36	−1.54	−0.87	6.82		
		3-9-2	4.48	0.09	78.48	−1.40	−0.88	6.77	6.80	0.02
	LHT25-3-cpx1′	3-8-2-1	4.60	0.09	78.99	−1.48	−0.89	6.98		
		3-8-2-2	4.72	0.09	78.90	−1.47	−0.90	7.10	7.04	0.04
	LHT25-3-cpx1	3-8-1-1	4.41	0.10	80.73	−1.77	−0.91	7.09		
		3-8-1-2	4.58	0.11	80.60	−1.74	−0.92	7.25		
		3-8-1-3	4.50	0.10	79.61	−1.58	−0.93	7.02	7.12	0.05

[a]IMF is instrumental mass fractionation.
[b]The instrumental drift, which is revealed by the bracketing measurements of standard mounted in the sample block and is calculated according to a linear relationship with time.
[c]These measured values were affected by the mineral inclusion and/or relief of mineral rim (see Figure S3).

which indicates that recycled crust or crustal derivatives with high $\delta^{18}O$ values must have been involved in their mantle sources [*Eiler et al*., 1997; *Eiler*, 2001]. The possible candidates specifically point to continental crust [*Eiler*, 2001], fluids/melts expelled from the subducted slab [*Auer et al*., 2009, and references therein; *Martin et al*., 2011] or oceanic crust that has experienced low-*T* (<350°C) water-rock interaction [*Muehlenbachs*, 1986; *Taylor and Sheppard*, 1986; *Eiler*, 2001] with or without marine sediments. Similar to the discussion of *Liu et al*. [2015a] for the origin of high cpx $\delta^{18}O$ values in Taihang basalts, the high (Nb/La)*n* (*n* represent primitive mantle normalization), Nb/U, and Ce/Pb ratios in our samples (Figure 3) argue against the significant role of continental crust ((Nb/La)*n*, Ce/Pb, and Nb/U ratios of the average continental crust are 0.4, 3.9, and 6.1, respectively [*Rudnick and Gao*, 2003]) or fluids expelled from the subducted slab because of their low corresponding values [*Tatsumi et al*., 1986; *Grove et al*., 2002] ((Nb/La)*n* ratios of fluids in the mantle wedge are always as low as 0.19–0.57, although the Ce/Pb ratio could be up to ~23). Thus, the high $\delta^{18}O$ values in our samples exclusively indicate the involvement of components from oceanic crust in the mantle sources. This is consistent with the previous suggestions from studies on Mg stable isotopes for the ZLGT basalts ($\delta^{26}Mg$ low to −0.6‰, usually attributed to marine carbonates [*Yang et al*., 2012]) and a more enriched $^{87}Sr/^{86}Sr$ at a given $\varepsilon Nd(t)$ value relative to the global MORB Sr-Nd isotopic trend for the LHT alkali basalts and PSK basanites (Figure 2c) [*Kuang et al*., 2012; *Zhang et al*., 2008].

5.3. The Temporal Variation of the Recycled ROC Components

In the following sections, we first compare the $\delta^{18}O$ values of the Late Cretaceous (PSK basanites) to late Cenozoic basalts in the southeast NCC with that of their hosted mantle-derived xenoliths, which helps us to identify how the ROC were incorporated into the upper mantle during this time period. We then focus on the temporal variation of $\delta^{18}O$ for cpx phenocrysts in the 106 to ~0 Ma basalts (e.g., LHT basalts, 70–60 Ma) from the northern margin of the NCC, which may provide a more convincing identification of the nature of recycled oceanic crust. Finally, some of the implications of these $\delta^{18}O$ data are discussed briefly.

5.3.1. Contrast $\delta^{18}O$ Between the Lithospheric Mantle and Basalts in SE NCC

As shown in Figure 7, the oxygen isotopic composition ($\delta^{18}O$) of the olivine phenocrysts in the Late Cretaceous PSK basanites (calculated from $\delta^{18}O_{cpx}$ from this study with $\Delta^{18}O_{cpx\text{-}ol} = 0.4‰$ [*Mattey et al*., 1994]) and the late Cenozoic alkali-tholeiitic basalts in the Suwan-Shandong region [*Zhang et al*., 2009; *Z. Xu et al*., 2012; *Wang et al*., 2011; *Liu et al*., 2015b] are mainly higher than and lower than the normal mantle value, respectively.

However, the lithospheric mantle at these two time periods shows the reverse $\delta^{18}O$ anomalies to their hosting basalts (Figure 7). The Late Cretaceous lithospheric mantle in the southeastern NCC was suggested to consist of a newly accreted fertile mantle and an overlying residual, old and refractory

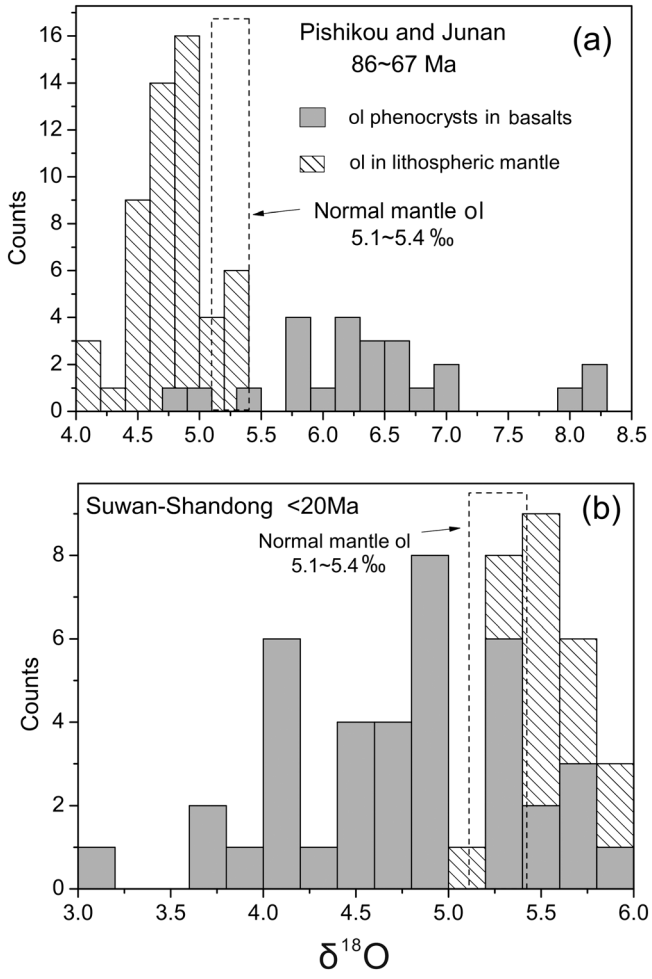

Figure 7. Comparison of the $\delta^{18}O$ of the olivine phenocrysts with that of olivine from the contemporaneous lithospheric mantle. The dashed vertical boxes mark the $\delta^{18}O$ range of olivine phenocrysts from N-MORB [*Eiler et al.*, 1997]. The $\delta^{18}O$ of olivine phenocrysts from PSK basanite are calculated from the $\delta^{18}O_{cpx}$ in this study and $\Delta^{18}O_{ol\text{-}cpx} = -0.4‰$ [*Mattey et al.*, 1994]. The $\delta^{18}O_{ol}$ for the Suwan-Shandong late Cenozoic basalts includes those calculated from $\delta^{18}O_{cpx}$ [*Liu et al.*, 2015b] and those from *Zhang et al.* [2009], *Wang et al.* [2011], and *Z. Xu et al.* [2012] (the data set with $\Delta^{18}O_{cpx\text{-}ol} < 0$ are filtered). The data of $\delta^{18}O_{ol}$ for 86–67 Ma and late Cenozoic NCC lithospheric mantle are from *Guo et al.*, 2013 and *Hao et al.*, 2015.

mantle [*Ying et al.*, 2006; *Zhang et al.*, 2011]. *Guo et al.* [2013] reported the low $\delta^{18}O$ (<5.4‰) of olivine as xenocrysts or in the peridotite hosted in Jünan and PSK basalts. These olivines with Mg# ranging from 87 to 89 indicate these samples would come from a fertile part of the lithospheric mantle [*Ying et al.*, 2006]. The authors explained these low $\delta^{18}O$ olivines as the separates from the mantle metasomatized or hybridized by the partial melts of a high-*T* hydrothermally altered ROC. This kind of metasomatized/hybridized production in the lithospheric mantle were widely suggested to be the source of Cenozoic basalts in NCC [*Zhang et al.*, 2009; *Z. Xu et al.*, 2012; *Wang et al.*, 2011; *Dai et al.*, 2016]. As the contrast, the late Cenozoic lithospheric mantle in Suwan-Shandong area has $\delta^{18}O$ higher than the normal mantle value (5.5‰ on average [*Hao et al.*, 2015]). The studied peridotite xenoliths show olivine Mg# from 89 to 91, and the calculated equilibrium temperature are from 900 to 1200°C [*Hao et al.*, 2015]. According to the typical Cenozoic geothermal gradient in eastern China [*Huang and Xu*, 2010], the depths of these xenoliths are estimated to be from 40 km to the spinel-garnet peridotite transition zone of ~65 km. This means that the high $\delta^{18}O$ should be the characteristics of large portion of the lithospheric mantle at this time period. The mechanism for the contrast $\delta^{18}O$ of lithospheric mantle in the Late Cretaceous and late Cenozoic time is not clear now, the possible reasons, however, would be (1) the oxygen isotopic anomalies were formed during the cooling and accretion process of the upwelling asthenosphere, which had contain some components derived from the subducted oceanic slab; and/or (2) the long-time metasomatism by the slab-derived fluids/melt, which has been suggested to explain the oxygen isotopic disequilibrium between opx, cpx, and olivines [*Hao et al.*, 2015]. Alternatively, these secular changes in $\delta^{18}O$ of lithospheric mantle may also reflect the spatial geochemical heterogeneity, considering that the Suwan-Shandong region is ~500 km away from the PSK region.

Overall, whatever the specific mechanism, the clearest information by this study is that in southeastern NCC, at Late Cretaceous and late Cenozoic, the oxygen isotopes of the basalts are distinct from that of the lithospheric mantle, which strongly indicate that these basalts were not derived from the lithospheric mantle. On the other hand, the secular changes in $\delta^{18}O$ anomaly for the lithospheric mantle and the contemporary basalts (Figure 7) could be best explained by that the components from the subducted Pacific slab (e.g., upper ROC versus lower ROC) were dynamically supplied to the upper mantle beneath

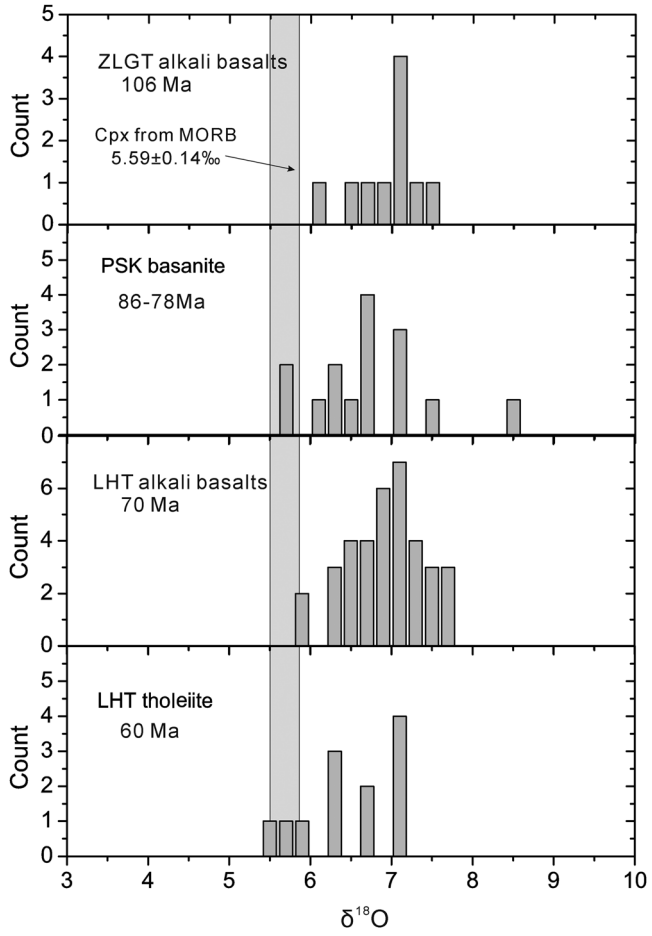

Figure 8. Histograms of $\delta^{18}O$ of cpx phenocrysts in the mafic rocks from 106 Ma to 60 Ma. All of the $\delta^{18}O$ values are for the single-spot analysis results. The light gray vertical box marks the $\delta^{18}O$ value for the cpx phenocrysts crystallized from N-MORB [*Eiler et al*., 1997].

the southeast NCC over a long time period. This means that the recycled oceanic components responsible for the OIB-type basalts in eastern China were not always having resided in the lithospheric mantle since the Early Cretaceous [*Zhang et al*., 2009; *Z. Xu et al*., 2012].

5.3.2. Evolution of the ROC Components in the Mantle Sources of 106 Ma to Late Cenozoic Basalts in the Northern Margin of NCC

Figure 8 illustrates the variation of $\delta^{18}O_{cpx}$ for the 106–60 Ma basalts. In Figure 9, companying with the published data of the Cenozoic basalts in the Central NCC and Southeastern NCC, the average $\delta^{18}O_{cpx}$ within each sample are compared with the bulk rock Ce/Pb, $^{87}Sr/^{86}Sr$, Ba/Th, and Nb/La ratios.

As shown in Figure 8, in the northern margin of NCC, the $\delta^{18}O_{cpx}$ of basalts from 106 Ma to 60 Ma are persistently significantly higher than that of the normal mantle. Due to the considerably low $\delta^{18}O$ of the altered lower oceanic crust (3.4‰ to 5.8‰ [*Gregory and Taylor*, 1981]), the generally high $\delta^{18}O$ of these samples indicate that the recycled components in the mantle sources were derived from the upper altered ROC. As shown in Figure 9, although the average $\delta^{18}O_{cpx}$ of basalt sample does not show any clear correlation with the bulk (Nb/La)*n*, Ba/Th, and $^{87}Sr/^{86}Sr$ ratios, the modeling shows that the high $\delta^{18}O_{cpx}$ of these basalts could be explained by the mixing of three end-member components, DMM, upper ROC and oceanic sediments. It could also be identified that the ZLGT basalts (106 Ma) have more contribution from the upper ROC than other younger counterparts, and both the alkali and tholeittic LHT basalts seem have similar portion of contribution from those two hybridized sources, which means that the sediments components relative to the ROC components are variable with time.

At the Late Cretaceous, the situation in Southeastern NCC seems a bit different from the case in the northern margin of NCC. As we have shown in Figure 7, although the basalts (PSK) show obvious contribution from upper ROC, the $\delta^{18}O$ of the lithospheric mantle (lower than the normal mantle value) indicates that some derivatives from lower ROC have been involved in the upper mantle before 87 Ma. From early Cenozoic on, the lower ROC components increasingly appeared in the mantle sources of basalts eastern China widely. The $\delta^{18}O$ of cpx in basalts in Shuangliao (51 Ma to 40 Ma [*Y. G. Xu et al*., 2012]), Northeast China, varies from 5.0 to 7.0‰ (basalts at 40 Ma have comparatively lower $\delta^{18}O_{cpx}$, from 4.0 to 6.0‰, *Chen* [2017]), which indicates that the upper and lower ROC have simultaneously played their roles in the mantle source. Such a situation was more extensive during the late Cenozoic. As shown in Figure 9, the nearly synchronical basalts in the Central NCC (Taihang and Chifeng 25 Ma–5.6 Ma and 25 Ma–2.5 Ma, respectively) and the southeastern NCC (Suwan-Shandong, $<$25 Ma) show obviously upper and lower ROC signatures, respectively. For Changle basalts, both upper and lower ROC have been involved in the source (Figures 9c and 9d).

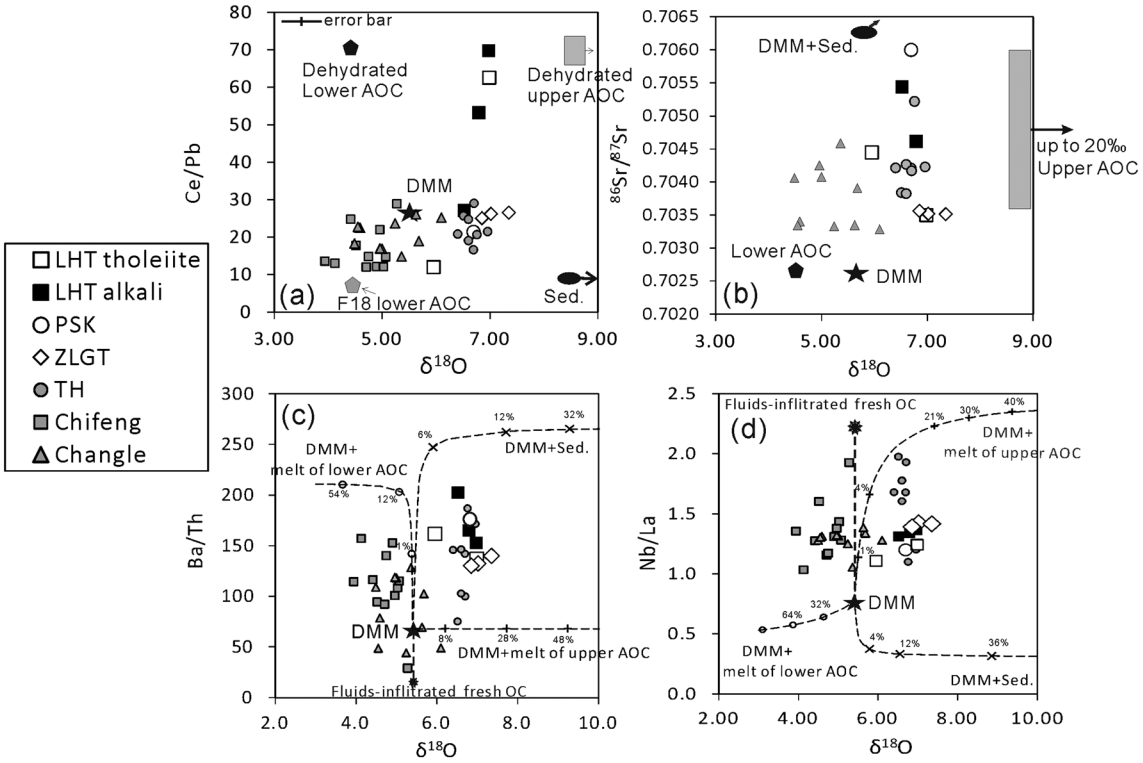

Figure 9. The comparison of oxygen isotopes of cpx with the (a, c, and d) bulk rock elemental ratios and (b) $^{87}Sr/^{86}Sr$. In Figure 9a, the Ce/Pb ratios of the dehydrated lower and upper ROC were calculated based on the mobility difference of these two elements [*Kessel et al*., 2005], and F18 is the sample number in *Bach et al*., 2001. In Figures 9c and 9d, the bold dashed lines show the modeled mixing among the depleted-MORB mantle (DMM) [*Workman and Hart*, 2005] and the marine sediments (Sed.) (GLOSS in *Plank and Langmuir* [1998]), partial melts of altered upper oceanic crust [*Staudigel et al*., 1995], and altered lower oceanic crust (AOC) [*Bach et al*., 2001]. The "fluids infiltrated fresh OC" means the oceanic crust effected by fluids but without of obvious change in oxygen isotopes [*Bach et al*., 2001]. Note that the elemental loss in the subduction process have been considered based on the elemental mobility during the hydration process in the subduction zone are from *Johnson and Plank* [1999] and *Kessel et al*. [2005]. The composition of the partial melting of the subducted oceanic crust was (eclogite) is calculated with the Excel sheet of *Stracke et al*. [2003]. The data for the Changle (Suwan-Shandong region) and Chifeng (northern margin of NCC) basalts are calculated from the $\delta^{18}O_{ol}$ by *Y. G. Xu et al*. [2012] and *Wang et al*. [2015], respectively, based on the equilibrium fractionation $\Delta^{18}O_{cpx\text{-}ol} = 0.4‰$ [*Mattey et al*., 1994]. Taihang basalt data are from *Liu et al*. [2015a].

Overall, the oxygen isotope data for the basalts from 106 Ma to ~0 Ma do not support a monotonous change of the recycled components from upper ROC to lower ROC in the mantle sources [*Kuang et al*., 2012; *Y. G. Xu et al*., 2012]. Instead, they also indicate a dynamical contribution from different part of Pacific oceanic crust.

6. Implications

The changes in composition for mantle-derived mafic rocks have usually been used to infer the thickness evolution of the NCC's lithospheric mantle [*Xu*, 2001; *Yan et al*., 2003, 2005; *Kuang et al*., 2012; *Xu*, 2014; *Zhang et al*., 2003]. One critical step in this performance is the estimation of the depth where partial melting occurred, which usually relies on the peridotite-based experimental results showing that alkali basalts (Si deficient) would derive from a deeper source than tholeiitic basalts (>3 GPa versus 1.5–2.5 GPa) [*Falloon et al*., 1988], or on the dependence of bulk FeO and Na_2O content on melting depth [*Langmuir et al*., 1992]. However, the validity of these discriminate criteria is counteracted by (1) the widespread appearance of ROC components in the mantle sources of the mafic rocks from 106 Ma to the late Cenozoic, most likely in the form of pyroxenite and eclogite (metamorphosed from MORB, or the secondary pyroxenite) [this work; *Zhang et al*., 2009; *Kuang et al*., 2012; *Z. Xu et al*., 2012; *Y. G. Xu et al*., 2012; *Zeng et al*., 2011; *Xu*, 2014; *Liu et al*., 2015a, 2015b]; (2) the fact that the partial melting of these fusible components could produce silicon-excessive/deficient melts [e.g., *Hirschmann et al*., 2003; *Sobolev et al*., 2007]; and (3) the interaction between the pyroxenite-/eclogite-derived melt and the surrounding ambient mantle, which could produce residual melts with silicon-excessive or silicon-deficient components [*Stracke and Bourdon*, 2009; *Mallik and Dasgupta*, 2012, 2014; *Lambart et al*., 2012].

In the "melting column" and the lithospheric lid effect model [*Klein and Langmuir*, 1987], the average melting depth of the upwelling asthenosphere (with ROC components) would be controlled by two factors at a given mantle temperature: the components of the mantle source and the thickness of the lithosphere. The mantle source with lower ROC is less fusible than the upper ROC and mainly fuses in a shallower mantle, because the lower ROC usually has higher MgO than the upper ROC and thus higher solidus temperature, and the intercept with mantle geotherm occurs at shallower depth [*Pertermann and Hirschmann*, 2003]. Following with model, *Kuang et al*. [2012] and *Y. G. Xu et al*. [2012] suggested that the secular increase in Eu/Eu* and a decrease in $^{87}Sr/^{86}Sr$ with time for the 90–40 Ma mafic rocks in the northern NCC and southern NEC (Northeast China) mirrored a shift in magma source from the upper to lower part of the ROC, which may finally reflect a continuous thinning of the lithospheric mantle from the Late Cretaceous to the early Cenozoic. However, as we have discussed in the last section, the $\delta^{18}O$ data in this study indicate that the recycled components in the mantle sources of basalts from 106 Ma to 60 Ma were dominantly upper ROC. In fact, the linkage between the Eu/Eu* variation of a basalt and the type of ROC in the source is not so direct. This can be best demonstrated by the observation that the recycled oceanic components in the mantle sources of the Cenozoic alkali basalts from Taihang mountain and West Shandong are upper and lower oceanic crust (their cpx $\delta^{18}O$ are higher and lower than that of the normal mantle, respectively [*Liu et al*., 2015a, 2015b]), respectively, while their bulk rocks do not exhibit corresponding negative and positive Eu anomalies [*Liu et al*., 2015a, 2015b]. Thus, the variation of Eu/Eu* and $^{87}Sr/^{86}Sr$ (and other geochemical indexes) could not be simply attributed to the shift from upper ROC to lower ROC components in the mantle sources and then used to suggest the thickness evolution of lithospheric mantle.

Zhang et al. [2009], *Z. Xu et al*. [2012], and *Dai et al*. [2016] have suggested that the ROC-derived components had been "frozen" in the "juvenile" lithospheric mantle since the Early Cretaceous and were responsible for the OIB-type basalts in the NCC from that time on. However, as discussed above, from 106 Ma to the late Cenozoic, the contribution of the ROC components into the upper mantle beneath the NCC was dynamic and alternating, which most likely came from the upwelling convective asthenosphere.

7. Conclusions

The $\delta^{18}O$ values of the cpx phenocrysts in the ZLGT basalts (106 Ma) and the LHT alkali-to-tholeiitic basalts (70–60 Ma) from the northern margin of the NCC and the PSK basanites (86–78 Ma) from the eastern NCC are all obviously higher than the normal mantle value. The data confirm that the recycled oceanic crust from the subducted Pacific oceanic slab were involved in the mantle sources of mafic rocks since 106 Ma. However, our data also clearly show the following:

1. The OIB-type mafic rocks in the NCC were most likely derived from the convective asthenosphere rather than from the lithospheric mantle.
2. From 106 Ma to 60 Ma, the recycled components in the northern NCC were dominantly upper ROC, and there was no visible temporal shift from upper ROC to lower ROC in the northern NCC.
3. In the southeast NCC, from the Late Cretaceous to the late Cenozoic, both upper and lower ROC were involved in the mantle sources, and these ROC components were incorporated into the source gradually and dynamically, rather than having resided in the lithospheric mantle since the Early Cretaceous.
4. The widespread involvement of ROC components in the mantle sources calls for more caution in the use of geochemical characteristics of basalts to infer the evolution of the lithosphere.

Acknowledgments
The data supporting this paper are available as supporting information. We thank Yi-Gang Xu, Wei Yang, and Shu-Guang Li for providing LHT and ZLGT basalt samples. We are also grateful to Jiang-Lin Xu, Juan Wang, and Yong-Hong Shi for their help in the EPMA analyses. The comments from Takeshi Kuritani and one anonymous reviewer and the suggestions from the Editor Michael Walter are much helpful to improve this paper. This work was funded by National Natural Science Foundation of China (41502041 and 41225005) and China Postdoctoral Science Foundation (2015M580542).

References

Auer, S., I. Bindecman, P. Wallace, V. Ponomareva, and M. Portnyagin (2009), The origin of hydrous, high-$\delta^{18}O$ voluminous volcanism: Diverse oxygen isotope values and high magmatic water contents within the volcanic record of Klyuchevskoy volcano, Kamchatka, Russia, *Contrib. Mineral. Petrol.*, *157*, 209–230.

Bach, W., J. C. Alt, Y. Niu, S. E. Humphris, J. Erzinger, and H. J. Dick (2001), The geochemical consequences of late-stage low-grade alteration of lower ocean crust at the SW Indian Ridge: Results from ODP Hole 735B (Leg 176), *Geochim. Cosmochim. Acta*, *65*(19), 3267–3287.

Cai, Y. C., H. R. Fan, M. Santosh, X. Liu, F. F. Hu, K. F. Yang, and Y. Liu (2013), Evolution of the lithospheric mantle beneath the southeastern North China Craton: Constraints from mafic dikes in the Jiaobei terrain, *Gondwana Res.*, *24*(2), 601–621.

Chen, H. (2017), The role of the Pacific subduction on the genesis of Cenozoic basalts in eastern China: New constrains from water content and oxygen isotope composition, PhD thesis, Univ. of Science and Technology of China, Hefei.

Chen, H., Q. K. Xia, J. Ingrin, Z. B. Jia, and M. Feng (2015), Changing recycled oceanic components in the mantle source of the Shuangliao Cenozoic basalts, NE China: New constraints from water content, *Tectonophysics*, *650*, 113–123.

Dai, L. Q., Y. F. Zheng, and Z. F. Zhao (2016), Termination time of peak decratonization in North China: Geochemical evidence from mafic igneous rocks, *Lithos*, *240*, 327–336.
Eiler, J. M. (2001), Oxygen isotope variations of basaltic lavas and upper mantle rocks, *Rev. Mineral. Geochem.*, *43*, 319–364.
Eiler, J. M., K. A. Farley, J. W. Valley, E. Hauri, H. Craig, S. R. Hart, and E. M. Stolper (1997), Oxygen isotope variations in ocean island basalt phenocrysts, *Geochim. Cosmochim. Acta*, *61*, 2281–2293.
Falloon, T. J., D. H. Green,C. J. Hatton, and K. L. Harris (1988), Anhydrous partial melting of a fertile and depleted peridotite from 2 to 30 kb and application to basalt petrogenesis, *J. Petrol.*, *29*(6), 1257–1282.
Fukao, Y., M. Obayashi, H. Inoue, and M. Nenbai (1992), Subducting slabs stagnant in the mantle transition zone, *J. Geophys. Res.*, *97*, 4809–4822, doi:10.1029/91JB02749.
Gao, S., R. L. Rudnick, W. L. Xu, H. L. Yuan, Y. S. Liu, R. J. Walker, and J. Yang(2008), Recycling deep cratonic lithosphere and generation of intraplate magmatism in the North China Craton, *Earth Planet. Sci. Lett.*, *270*(1), 41–53.
Gregory, R. T., and H. P. Taylor (1981), An oxygen isotope profile in a section of Cretaceous oceanic crust, Samail Ophiolite, Oman: Evidence for $\delta^{18}O$ buffering of the oceans by deep (>5 km) seawater-hydrothermal circulation at mid-ocean ridges, *J. Geophys. Res.*, *86*(B4), 2737–2755, doi:10.1029/JB086iB04p02737.
Grove, T., S. Parman, S. Bowring, R. Price, and M. Baker (2002), The role of an H_2O-rich fluid component in the generation of primitive basaltic andesites and andesites from the Mt. Shasta region, N California, *Contrib. Mineral. Petrol.*, *142*(4), 375–396.
Guo, F., J. Guo, Y. Wang, W. Fan, C. Li, H. Li, and L. Zhao (2013), A metasomatized mantle wedge origin for low-δ 18O olivine in late Cretaceous Junan and Qingdao basalts in the Sulu orogen, *Chin. Sci. Bull.*, *58*(32), 3903–3913.
Guo, P., Y. Niu, L. Ye, J. Liu, P. Sun, H. Cui, and Y. Feng (2014), Lithosphere thinning beneath west North China Craton: Evidence from geochemical and Sr–Nd–Hf isotope compositions of Jining basalts, *Lithos*, *202*, 37–54.
Gurenko, A. A., M. Chaussidon, and H. U. Schmincke (2001), Magma accent and contamination beneath one intraplate volcano: Evidence from S and O isotopes in glass inclusions and their host clinopyroxenes from Miocene basaltic yaloclastites southwest of Gran Canaria (Canary Islands), *Geochim. Cosmochim. Acta*, *65*, 4359–4374.
Gurenko, A. A., I. N. Bindeman, and M. Chaussidon (2011), Oxygen isotope heterogeneity of the mantle beneath the Canary Islands: Insights from olivine phenocrysts, *Contrib. Mineral. Petrol.*, *162*, 349–363.
Hao, Y. T., Q. K. Xia, L. Dallai, and M. Coltorti (2015), Recycled oceanic crust-derived fluids in the lithospheric mantle of eastern China: Constraints from oxygen isotope compositions of peridotite xenoliths, *Lithos*, *228*, 55–61.
Hirschmann, M. M., T. Kogiso, M. B. Baker, and E. M. Stolper (2003), Alkalic magmas generated by partial melting of garnet pyroxenite, *Geology*, *31*(6), 481–484.
Hofmann, A. W., K. P. Jochum, M. Seufert, and W. M. White (1986), Nb and Pb in oceanic basalts: New constraints on mantle evolution, *Earth Planet. Sci. Lett.*, *79*(1–2), 33–45.
Huang, J., and D. Zhao (2006), High-resolution mantle tomography of China and surrounding regions, *J. Geophys. Res.*, *111*, B09305, doi:10.1029/2005JB004066.
Huang, X. L., J. W. Zhong, and Y. G. Xu (2012), Two tales of the continental lithospheric mantle prior to the destruction of the North China Craton: Insights from Early Cretaceous mafic intrusions in western Shandong, East China, *Geochim. Cosmochim. Acta*, *96*, 193–214.
Huang, X., and Y. G. Xu (2010), Thermal state and structure of the lithosphere beneath eastern china: A synthesis on basalt-borne xenoliths, *J. Earth Sci.*, *21*(5), 711–730.
Johnson, M. C., and T. Plank (1999), Dehydration and melting experiments constrain the fate of subducted sediments, *Geochem. Geophys. Geosyst.*, *1*(12), 597–597, doi:10.1029/1999GC000014.
Kessel, R., M. W. Schmidt, P. Ulmer, and T. Pettke (2005), Trace element signature of subduction-zone fluids, melts and supercritical liquids at 120–180 km depth, *Nature*, *437*(7059), 724–7.
Klein, E. M., and C. H. Langmuir (1987), Global correlations of ocean ridge basalt chemistry with axial depth and crustal thickness, *J. Geophys. Res.*, *92*(B8), 8089–8115, doi:10.1029/JB092iB08p08089.
Kuang, Y. S., X. Wei, L. B. Hong, J. L. Ma, C. J. Pang, Y. T. Zhong, J.-X. Zhao, and Y. G. Xu (2012), Petrogenetic evaluation of the Laohutai basalts from North China Craton: Melting of a two-component source during lithospheric thinning in the late Cretaceous–early Cenozoic, *Lithos*, *154*, 68–82.
Lambart, S., D. Laporte, A. Provost, and P. Schiano (2012), Fate of pyroxenite-derived melts in the peridotitic mantle: Thermodynamic and experimental constraints, *J. Petrol.*, *53*(3), 451–476.
Langmuir, C., E. M. Klein, T. Plank (Eds.) (1992), Petrological systematics of mid-ocean ridge basalts: Constraints on melt generation beneath ocean ridges, AGU, pp. 183–280.
Liu, J., Q. K. Xia, E. Deloule, H. Chen, and M. Feng (2015a), Recycled oceanic crust and marine sediment in the source of alkali basalts in Shandong, eastern China: Evidence from magma water content and oxygen isotopes, *J. Geophys. Res. Solid Earth*, *120*, 8281–8303, doi:10.1002/2015JB012476.
Liu, J., Q. K. Xia, E. Deloule, J. Ingrin, H. Chen, and M. Feng (2015b), Water content and oxygen isotopic composition of alkali basalts from the Taihang Mountains, China: Recycled oceanic components in the mantle source, *J. Petrol.*, egv013.
Liu, Y., S. Gao, P. B. Kelemen, and W. Xu (2008), Recycled crust controls contrasting source compositions of Mesozoic and Cenozoic basalts in the North China Craton, *Geochim. Cosmochim. Acta*, *72*, 2349–2376.
Liu, S. C., Q. K. Xia, S. H. Choi, E. Deloule, P. Li, and J. Liu (2016), Continuous supply of recycled Pacific oceanic materials in the source of Cenozoic basalts in SE China: The Zhejiang case, *Contrib. Mineral. Petrol.*, *171*(12), 100, doi:10.1007/s00410-016-1310-4.
Ma, L., S. Y. Jiang, A. W. Hofmann, B. Z. Dai, M. L. Hou, K. D. Zhao, L.-H. Chen, J.-W. Li, and Y. H. Jiang (2014), Lithospheric and asthenospheric sources of lamprophyres in the Jiaodong Peninsula: A consequence of rapid lithospheric thinning beneath the North China Craton? *Geochim. Cosmochim. Acta*, *124*, 250–271.
Mallik, A., and R. Dasgupta (2012), Reaction between MORB-eclogite derived melts and fertile peridotite and generation of ocean island basalts, *Earth Planet. Sci. Lett.*, *329*, 97–108.
Mallik, A., and R. Dasgupta (2014), Effect of variable CO2 on eclogite-derived andesite and lherzolite reaction at 3 GPa—Implications for mantle source characteristics of alkalic ocean island basalts, *Geochem. Geophys. Geosyst.*, *15*, 1533–1557, doi:10.1002/2014GC005251.
Martin, E., I. Bindeman, and T. L. Grove (2011), The origin of high-Mg magmas in Mt Shasta and Medicine Lake volcanoes, Cascade Arc (California): Higher and lower than mantle oxygen isotope signatures attributed to current and past subduction, *Contrib. Mineral. Petrol.*, *162*, 945–960.
Mattey, D., D. Lowry, and C. Macpherson (1994), Oxygen isotope composition of mantle peridotite, *Earth Planet. Sci. Lett.*, *128*, 231–241.
Mcdonough, W. F., and S. S. Sun (1995), The composition of the Earth, *Chem. Geol.*, *120*(3–4), 223–253.

Meng, F. X., S. Gao, Y. L. Niu, Y. S. Liu, and X. R. Wang (2015), Mesozoic-Cenozoic mantle evolution beneath the North China Craton: A new perspective from Hf-Nd isotopes of basalts, *Gondwana Res.*, doi:10.1016/j.gr.2014.01.014.
Muehlenbachs, K. (1986), Alteration of the oceanic crust and the ^{18}O history of seawater, *Rev. Mineral. Geochem.*, *16*(1), 425–444.
Niu, Y. L. (2005), Generation and evolution of basaltic magmas: Some basic concepts and a new view on the origin of Mesozoic–Cenozoic basaltic volcanism in eastern China, *Geol. J. China Univ.*, *11*, 9–46.
Pang, C. J., X. C. Wang, Y. G. Xu, S. N. Wen, Y. S. Kuang, and L. B. Hong (2015), Pyroxenite-derived Early Cretaceous lavas in the Liaodong Peninsula: Implication for metasomatism and thinning of the lithospheric mantle beneath North China Craton, *Lithos*, *227*, 77–93.
Pertermann, M., and M. M. Hirschmann, (2003), Partial melting experiments on a MORB-like pyroxenite between 2 and 3 GPa: Constraints on the presence of pyroxenite in basalt source regions from solidus location and melting rate, *J. Geophys. Res.*, *108*(B2), 2125, doi:10.1029/2000JB000118.
Plank, T., and C. H. Langmuir (1998), The chemical composition of subducting sediment and its consequences for the crust and mantle, *Chem. Geol.*, *145*(3–4), 325–394.
Putirka, K. D., H. Mikaelian, F. Ryerson, and H. Shaw (2003), New clinopyroxene-liquid thermobarometers for mafic, evolved, and volatile-bearing lava compositions, with applications to lavas from Tibet and the Snake River Plain, Idaho, *Am. Mineral.*, *88*(10), 1542–1554.
Rudnick, R. L., and S. Gao (2003), Composition of the continental crust, *Treatise Geochem.*, *3*, 1–64.
Sakuyama, T., W. Tian, J.-I. Kimura, Y. Fukao, Y. Hirahara, T. Takahashi, R. Senda, Q. Chang, T. Miyazaki, and M. Obayashi (2013), Melting of dehydrated oceanic crust from the stagnant slab and of the hydrated mantle transition zone: Constraints from Cenozoic alkaline basalts in eastern China, *Chem. Geol.*, *359*, 32–48.
Song, Y., F. A. Frey, and X. Zhi (1990), Isotopic characteristics of Hannuoba basalts, eastern China: Implications for their petrogenesis and the composition of subcontinental mantle, *Chem. Geol.*, *88*(1), 35–52.
Sobolev, A. V., et al. (2007), The amount of recycled crust in sources of mantle-derived melts, *Science*, *316*(5823), 412–417.
Staudigel, H., G. R. Davies, S. R. Hart, K. M. Marchant, and B. M. Smith (1995), Large scale isotopic Sr, Nd and O isotopic anatomy of altered oceanic crust: DSDP/ODP sites417/418, *Earth Planet. Sci. Lett.*, *130*(1–4), 169–185.
Stracke, A., and B. Bourdon (2009), The importance of melt extraction for tracing mantle heterogeneity, *Geochim. Cosmochim. Acta*, *73*(1), 218–238.
Stracke, A., M. Bizimis, and V. J. M. Salters, (2003), Recycling oceanic crust: Quantitative constraints, *Geochem. Geophys. Geosyst.*, *4*(3), 8003, doi:10.1029/2001GC000223.
Tatsumi, Y., D. L. Hamilton, and R. W. Nesbitt (1986), Chemical characteristics of fluid phase released from a subducted lithosphere and origin of arc magmas: Evidence from high-pressure experiments and natural rocks, *J. Volcanol. Geotherm. Res.*, *29*, 293–309.
Taylor, H. P., and S. M. F. Sheppard (1986), Igneous rocks: I. Processes of isotopic fractionation and isotope systematics, *Rev. Mineral. Geochem.*, *16*, 227–271.
Wang, X. C., S. A. Wilde, Q. L. Li, and Y. N. Yang (2015), Continental flood basalts derived from the hydrous mantle transition zone, *Nat. Commun.*, *6*, doi:10.1038/ncomms8700.
Wang, Y., Z.-F. Zhao, Y.-F. Zheng, and J.-J. Zhang (2011), Geochemical constraints on the nature of mantle source for Cenozoic continental basalts in east-central China, *Lithos*, *125*, 940–955.
Widom, E., and J. Farquhar (2003), Oxygen isotope signatures in olivines from Sao Miguel (Azores) basalts: Implications for crustal and mantle processes, *Chem. Geol.*, *193*, 237–255.
Winpenny, B., and J. Maclennan (2014), Short length scale oxygen isotope heterogeneity in the Icelandic mantle: Evidence from plagioclase compositional zones, *J. Petrol.*, *55*(12), 2537–2566.
Workman, R. K., and S. R. Hart (2005), Major and trace element composition of the depleted MORB mantle (DMM), *Earth Planet. Sci. Lett.*, *231*(1–2), 53–72.
Xia, Q.-K., L. Dallai, and E. Deloule (2004), Oxygen and hydrogen isotope heterogeneity of clinopyroxene megacrysts from Nushan Volcano, SE China, *Chem. Geol.*, *209*, 137–151.
Xia, Q.-K., J. Liu, S.-C. Liu, I. Kovacs, M. Feng, and L. Dang (2013), High water content in Mesozoic primitive basalts of the North China Craton and implications on the destruction of cratonic mantle lithosphere, *Earth Planet. Sci. Lett.*, *361*, 85–97.
Xu, Y. G. (2007), Diachronous lithospheric thinning of the North China Craton and formation of the Daxin'anling–Taihangshan gravity lineament, *Lithos*, *96*(1), 281–298.
Xu, Y. G. (2014), Recycled oceanic crust in the source of 90–40Ma basalts in North and Northeast China: Evidence, provenance and significance, *Geochim. Cosmochim. Acta*, *143*, 49–67.
Xu, Y. G., H. H. Zhang, H. N. Qiu, W. C. Ge, and F. Y. Wu (2012), Oceanic crust components in continental basalts from Shuangliao, Northeast China: Derived from the mantle transition zone?, *Chem. Geol.*, *328*, 168–184.
Xu, Y.-G. (2001), Thermo-tectonic destruction of the Archaean lithospheric keel beneaththe Sino-Korean craton in China: Evidence, timing and mechanism, *Phys. Chem. Earth (A)*, *26*, 747–757.
Xu, Y.-G., H. Y. Li, C. J. Pang, and B. He (2009), On the timing and duration of the destruction of the North China Craton, *Chin. Sci. Bull.*, *54*, 1974–1989.
Xu, Z., Z.-F. Zhao, and Y.-F. Zheng (2012), Slab–mantle interaction for thinning of cratonic lithospheric mantle in North China: Geochemical evidence from Cenozoic continental basalts in central Shandong, *Lithos*, *146*, 202–217.
Yan, J., J. F. Chen, and Z. Xie (2003), Mantle xenoliths from Late Cretaceous basalt in eastern Shandong Province: New constraint on the timing of lithospheric thinning in eastern China, *Chin. Sci. Bull.*, *48*, 2139–2144.
Yan, J., J. F. Chen, Z. Xie, T. S. Gao, K. A. Foland, X. D. Zhang, and M. W. Liu (2005), Studies on petrology and geochemistry of the late Cretaceous basalts and mantle-derived xenoliths from eastern Shandong, *Acta Petrol. Sin.*, *21*, 99–112.
Yang, W., and S. Li (2008), Geochronology and geochemistry of the Mesozoic volcanic rocks in Western Liaoning: Implications for lithospheric thinning of the North China Craton, *Lithos*, *102*(1), 88–117.
Yang, W., F.-Z. Teng, H.-F. Zhang, and S.-G. Li (2012), Magnesium isotopic systematics of continental basalts from the North China craton: Implications for tracing subducted carbonate in the mantle, *Chem. Geol.*, *328*, 185–194.
Ying, J., H. Zhang, N. Kita, Y. Morishita, and G. Shimoda (2006), Nature and evolution of late cretaceous lithospheric mantle beneath the eastern north china craton: Constraints from petrology and geochemistry of peridotitic xenoliths from Jünan, Shandong Province, China, *Earth Planet. Sci. Lett.*, *244*(3–4), 622–638.
Zeng, G., L.-H. Chen, A. W. Hofmann, S.-Y. Jiang, and X.-S. Xu (2011), Crust recycling in the sources of two parallel volcanic chains in Shandong, North China, *Earth Planet. Sci. Lett.*, *302*, 359–368.
Zhang, H. F., M. Sun, X. H. Zhou, W. M. Fan, M. G. Zhai, and J. F. Yin (2002), Mesozoic lithosphere destruction beneath the North China Craton: Evidence from major-, trace-element and Sr–Nd–Pb isotope studies of Fangcheng basalts, *Contrib. Mineral. Petrol.*, *144*(2), 241–254.

Zhang, H. F., M. Sun, X. H. Zhou, M. F. Zhou, W. M. Fan, and J. P. Zheng (2003), Secular evolution of the lithosphere beneath the eastern North China Craton: Evidence from Mesozoic basalts and high-Mg andesites, *Geochim. Cosmochim. Acta*, *67*(22), 4373–4387.

Zhang, J., H. F. Zhang, J. F. Ying, Y. J. Tang, and L. F. Niu (2008), Contribution of subducted Pacific slab to Late Cretaceous mafic magmatism in Qingdao region, China: A petrological record, *Island Arc*, *17*(2), 231–241.

Zhang, J., H. F. Zhang, N. Kita, G. Shimoda, Y. Morishita, J. Ying, and Y. Tang (2011), Secular evolution of the lithospheric mantle beneath the eastern North China craton: Evidence from peridotitic xenoliths from Late Cretaceous mafic rocks in the Jiaodong region, east-central China, *Int. Geol. Rev.*, *53*, 182–211.

Zhang, J.-J., Y.-F. Zheng, and Z.-F. Zhao (2009), Geochemical evidence for interaction between oceanic crust and lithospheric mantle in the origin of Cenozoic continental basalts in east-central China, *Lithos*, *110*, 305–326.

Zhao, D. (2004), Global tomographic images of mantle plumes and subducting slabs: Insight into deep Earth dynamics, *Phys. Earth Planet. Inter.*, *146*(1), 3–34.

Zhao, G., and M. Zhai (2013), Lithotectonic elements of Precambrian basement in the North China Craton: Review and tectonic implications, *Gondwana Res.*, *23*(4), 1207–1240.

Zhao, Z. F., and Y. F. Zheng (2003), Calculation of oxygen isotope fractionation in magmatic rocks, *Chem. Geol.*, *193*, 59–80.

Zhi, X., Y. Song, F. A. Frey, J. Feng, and M. Zhai (1990), Geochemistry of Hannuoba basalts, eastern China: Constraints on the origin of continental alkalic and tholeiitic basalt, *Chem. Geol.*, *88*, 1–33.

Zhu, R. X., L. Chen, F. Y. Wu, and J. L. Liu (2011), Timing, scale and mechanism of the destruction of the North China Craton, *Sci. China Earth Sci.*, *54*, 789–797.